Exploring the Drivers of Tropospheric Hydroxyl Radical Trends in the GFDL AM4.1 Atmospheric Chemistry-Climate Model

Glen Chua[1,2], Vaishali Naik[2], and Larry Horowitz[2]

[1]Princeton University, Program in Atmospheric and Oceanic Science
[2]NOAA Geophysical Fluid Dynamics Laboratory, Princeton, NJ, USA

Correspondence: Glen Chua (gchua@princeton.edu)

Abstract.

We explore the sensitivity of modelled tropospheric hydroxyl (OH) concentration trends to meteorology and near-term climate forcers (NTCFs), namely methane (CH_4); nitrogen oxides ($NO_x = NO_2 + NO$); carbon monoxide (CO); non-methane volatile organic compounds (NMVOCs); and ozone-depleting substances (ODS) using the Geophysical Fluid Dynamics Laboratory (GFDL)'s atmospheric chemistry-climate model, Atmospheric Model version 4.1 (AM4.1) driven by emissions inventories developed for the Sixth Coupled Model Intercomparison Project (CMIP6) and forced by observed sea surface temperatures and sea ice prepared in support of the CMIP6 Atmospheric Model Intercomparison Project (AMIP) simulations. We find that the modelled tropospheric airmass-weighted mean [OH] has increased by $\sim 5\%$ globally from 1980 to 2014. We find that NO_x emissions and CH_4 concentrations dominate the modelled global trend, while CO emissions and meteorology were also important in driving regional trends. Modelled tropospheric NO_2 column trends are largely consistent with those retrieved from the Ozone Monitoring Instrument (OMI) satellite, but simulated CO column trends generally overestimate those retrieved from the Measurements of Pollution in The Troposphere (MOPITT) satellite, possibly reflecting biases in input anthropogenic emission inventories, especially over China and South Asia.

1 Introduction

The hydroxyl radical (OH), as the primary daytime oxidant in the troposphere (Levy, 1971), plays an important role in atmospheric chemistry. OH influences air quality and climate, as reaction with OH is a major sink of various trace species including tropospheric ozone precursors such as methane (CH_4), carbon monoxide (CO), nitrogen oxides ($NOx = NO + NO_2$), ozone-depleting substances (ODS) such as halocarbons, and non-methane volatile organic compounds (NMVOCs) (e.g. Holmes et al. (2013); Turner et al. (2019)). Precise knowledge of the OH budget, its variations and trends, and its response to various drivers, is needed to determine source and sink budgets for these important trace species, and is therefore crucial to our understanding of the various aforementioned effects on the Earth system (e.g. Lawrence et al., 2001; Naik et al., 2013; Murray et al., 2014; Zhao et al., 2019; Nicely et al., 2020; Patra et al., 2021). In particular, there are still gaps in our understanding of the drivers of the observed atmospheric methane concentration growth rate in recent years (Saunois et al., 2020; Nisbet et al., 2021), further highlighting the importance of better understanding [OH] trends and variability. Recent observational based studies suggest

Table 1. Important reactions describing tropospheric OH chemistry.

Reaction number	Reaction
R1	$O_3 + h\nu \rightarrow O(^1D) + O_2, \lambda < 330nm$
R2	$O(^1D) + H_2O \rightarrow 2OH$
R3	$HO_2 + NO \rightarrow NO_2 + OH$
R4	$O_3 + HO_2 \rightarrow 2O_2 + OH$
R5	$H_2O_2 + h\nu \rightarrow 2OH, \lambda < 550nm$
R6	$CO + OH(+O_2) \rightarrow HO_2 + CO_2$
R7	$RH + OH(+O_2) \rightarrow RO_2 + H_2O(+O_2)$
R8	$RO_2 + NO(+M) \rightarrow R'CHO + NO_2 + OH(+M)$
R9	$NO_2 + h\nu \rightarrow O(^3P) + NO, \lambda < 430nm$
R10	$O(^3P) + O_2(+M) \rightarrow O_3(+M)$
R11	$NO_2 + OH(+M) \rightarrow HNO_3(+M)$
R12	$HO_2 + HO_2 \rightarrow H_2O_2 + O_2$
R13	$RO_2 + HO_2 \rightarrow ROOH + O_2$

25 either a decline or stable OH concentrations over the past four decades (e.g. Rigby et al., 2017; Turner et al., 2017; Zhao et al., 2019) while global chemistry-climate models simulate increases over the same period (e.g Stevenson et al., 2020; Zhao et al., 2020). In this study, we employ the state-of-the-science GFDL chemistry-climate model (CCM), AM4.1, to systematically explore the drivers of changes in [OH] between 1980 and 2014 to shed light on its role in driving recent methane increases.

Changes in [OH] can be traced back to changes in the budget terms. The time tendency of [OH] is determined by the 30 balance between chemical production (P) and loss (L) terms, since the chemical processes for OH tend to occur at much faster timescales compared to other potential terms in the budget equation such as advection and transport (Lelieveld et al., 2016). The governing time tendency equation therefore is given by

$$\frac{d[OH]}{dt} = P - L \tag{1}$$

Table 1 summarises the tropospheric OH chemistry that is described here. Primary production of tropospheric OH occurs 35 via the photodissociation of troposheric ozone (O_3) by ultraviolet (UV) radiation of wavelength less than 310 nm (R1) to produce excited singlet oxygen atoms ($O(^1D)$) (Brasseur and Solomon, 2005), which then react with water vapor (R2). OH can also be generated by secondary production mechanisms that recycle OH from hydroperoxy radicals (HO_2) (reactions R3-R5). In high-NOx regions, such as polluted urban environments, HO_2 can be recycled back to OH via reaction with NO without consuming O_3 (R3) and is the dominant production term. This NO_x-driven secondary prodution of OH, otherwise known as 40 the NO_x recycling mechanism of OH, is similar in magnitude to the primary formation of OH on a global basis, being about $\sim 30\%$ each (Lelieveld et al., 2016). In unpolluted regions, other secondary production mechanisms, collectively called the O_x recycling mechanism, are dominant. One involves the consumption of ozone in unpolluted regions (R4) (as opposed to

the production of ozone in polluted conditions), and the other involves the photolysis of H_2O_2 (R5). Oxidation of CO is the largest OH loss reaction (R6) with important losses via oxidation of methane and non-methane volatile organic compounds (NMVOCs) (R7). Organic peroxy radicals can also undergo an OH-recycling reaction with NO to form NO_2 (R8). The fate of the resultant organic carbon product, $R'CHO$, can be to either further generate OH or HO_2 radicals if it undergoes photolysis, or to undergo further oxidation by OH. The NO_2 produced via Reactions R3 and R8 can then be photolysed to form ozone (R9-R10), which then leads to further primary production of OH via Reactions R1 and R2 (Hameed et al., 1979). In a strongly polluted atmosphere, NO_2 can locally become a large HO_x ($HO_x = OH + HO_2$) sink, causing net OH loss through the formation of nitric acid (HNO_3) (R11) which can be washed out via wet deposition (Crutzen and Lawrence, 2000). Meanwhile, in clean, non-polluted conditions, the reaction chains involving the HO_2 and RO_2 radicals can be terminated via loss reactions R12 and R13. The self-reaction of HO_2 (R12) represents an OH sink, as the hydrogen peroxide (H_2O_2) product can be washed out via wet deposition and is the dominant HO_x sink since most of the troposphere experiences low NOx conditions (Jaeglé et al., 2001).

Overall, the atmospheric composition directly impacts the OH budget, most notably via tropospheric ozone, humidity, NO_x, CO, methane and NMVOCs, with the former three usually acting to increase [OH], and the latter three acting to decrease [OH], but there are also meteorological factors which influence the budget via influencing the tropospheric chemistry of OH as well. Temperature plays an important role in controlling rate reaction rates, tropospheric water vapour abundance and also natural emissions of biogenic VOCs (Spivakovsky et al., 2000). Also, as many important reactions are photolysis reactions, such as the primary production of OH via R1 which requires UV radiation of wavelengths ($\lambda < 330\text{nm}$), the overhead ozone column, which controls the amount of UV radiation penetrating into the troposphere, aerosol direct and indirect effects, and cloud cover play an important role as well (Levy, 1971). These point to the possible anthropogenic impacts on the OH budget which can impact these various factors directly or indirectly.

Because OH is highly reactive and therefore has a short lifetime of $\sim 1\text{s}$, this makes it difficult to achieve global observational coverage over time of directly-observed [OH]. As a result, various observational proxies have been used to indirectly estimate the spatial distribution, global mean as well as the temporal variations and trends of [OH]. A widely-used proxy is methyl chloroform (CH_3CCl_3, MCF) (e.g. Montzka et al., 2011; Rigby et al., 2017; Turner et al., 2017; Naus et al., 2019; Patra et al., 2021), for which there is a relatively long temporal observational record, for example the ~ 4 decades' worth of data from the Advanced Global Atmospheric Gases Experiment (AGAGE) and National Oceanic and Atmospheric Administration (NOAA) networks. Using a multi-box model inversion method, Rigby et al. (2017) and Turner et al. (2017) found an increasing global mean [OH] trend from the 1990s up to the mid-2000s but found a decreasing [OH] trend thereafter; however, in these studies, it was highlighted that the inferred [OH] trends were only weakly constrained, and when Naus et al. (2019) corrected for biases in the multi-box model inversion method, they found an overall increasing trend over the last 2 decades. To avoid some of these biases such as those arising from the spatial averaging required in box model methods, 3D chemistry transport models (CTMs) have also been used to infer [OH] from MCF observations such as in Patra et al. (2021) and Naus et al. (2021) who found no significant trend in [OH]. Non-MCF methods have also been used to explore [OH] trends since 1980: for example, Nicely et al. (2018) used observational constraints of various [OH] drivers to empirically reconstruct [OH], and found no significant

trend as well. Overall, global mean [OH] derived from most atmospheric inversions or empirical reconstructions seems to not have a significant trend over the 1980-2014 period. Models such as CTMs, CCMs and earth system models (ESMs) can also be used to calculate [OH], and these models have shown an increase in global mean [OH] since 1980 to present-day, in contrast to the [OH] trends derived from observational constraints (Naik et al., 2013; Zhao et al., 2019; Nicely et al., 2020; Stevenson et al., 2020; Zhao et al., 2020). Most of these studies found that changes to Near-term Climate Forcers (NTCFs) played a key role in driving the modelled [OH] increase. In particular, Stevenson et al. (2020) found an $\sim 10\%$ increase with respect to the 1998-2007 mean from 1980 to 2014 from 3 Earth System Models (ESMs) participating in the Aerosols and Chemistry Model Intercomparison Project (AerChemMIP) as part of the Sixth Coupled Model Intercomparison Project (CMIP6). They attribute this simulated increase to changes in anthropogenic NTCFs, mainly increases in anthropogenic nitrogen oxides combined with declining CO emissions since 1990 with smaller contributions from changes in halocarbon and aerosol-related emissions. Naik et al. (2013) and Nicely et al. (2020) also additionally highlight the role of stratospheric ozone loss due to factors such as emissions of ozone-depleting substances (ODS) and increasing specific humidity in driving the increasing [OH] trend.

As discussed above, there are a plethora of emissions-related, chemical and physical drivers that affect [OH], and many of these are also driven by climate variability (Alexander and Mickley, 2015). As such, [OH] tends to exhibit interannual variability (IAV), and various modelling studies have explored the drivers of [OH] IAV. For example, large-scale climate variability through the El Niño Southern Oscillation (ENSO) has been shown to play an important role in driving [OH] IAV, through ENSO effects on variability in: temperature and humidity (Zhao et al., 2020); biomass burning emissions such as CO (an OH sink) and NO_x (tends to enhance OH) (Holmes et al., 2013; Zhao et al., 2020); O_3 and $j(O^1D)$ in the lower troposphere (Anderson et al., 2021); and lightning NO_x emissions (Turner et al., 2018). In particular, the role of lightning NO_x in driving [OH] IAV in the GFDL AM4.1 over the period 1980-2016 was also highlighted by He et al. (2021), and Murray et al. (2013) who found that lightning NO_x emissions were the key factor driving IAV especially over the period 1998-2006 through its role in affecting both seconday OH production via the NO_x recycling mechanism as well as primary production via its role as a tropospheric ozone precursor. However, the drivers of OH variability also show large model diversity. For example, lightning NO_x can be parameterised differently in different models (Zhao et al., 2020; Wild et al., 2020), and so its response to climate variability like ENSO can vary from model to model.

In summary, in the period 1980-2014, global CCMs seem to have converged on an overall increasing [OH] trend driven by complementary changes in emissions and meteorology (Szopa et al., 2021). Here we build on previous studies to explore the contribution of individual component drivers to attribute trends and variability in [OH]. We apply the the GFDL-AM4.1 CCM to systematically explore the roles of meteorology and individual chemical drivers in changing [OH], with the goal of identifying the primary drivers of increasing [OH] trends over 1980-2014 simulated by global models. Additionally, we analyse the model simulations to shed light on the primary drivers of [OH] IAV.

2 Methods

2.1 GFDL AM4.1 Model Setup

We use the GFDL Atmospheric Model 4.1 (AM4.1), which is the atmosphere-only configuration of the GFDL Earth System Model ESM4.1. Further details of the AM4.1 setup are described by Horowitz et al. (2020), and a summary of the features relevant to [OH] are provided here. The AM4.1 has a spatial resolution of ~ 100km on a cubed-sphere grid, and resolves 49 vertical levels up to ~ 80km. It uses an updated chemical mechanism (Horowitz et al., 2020) with gas-phase and heterogeneous chemistry updates following Mao et al. (2013a, b). The key feature of this model configuration is that it has online oxidants, i.e. it includes chemical and climate feedbacks on oxidant concentrations. Photolysis rate constants are calculated interactively via the photolysis mechanism Fast-JX version 7.1 (Wild et al., 2000; Bian and Prather, 2002). All model simulations are forced with interannually varying sea surface temperatures and sea ice from Taylor et al. (2000), prepared in support of the Atmospheric Model Intercomparison Project (AMIP) simulations as part of phase 6 of the Coupled Model Intercomparison Project (CMIP6).

We used historical emissions datasets for ozone and aerosol precursors developed in support of CMIP6: the Community Emissions Database (CEDS) for anthropogenic emissions (v2017-05-18; Hoesly et al. (2018)) and historical biomass burning emissions for CMIP6 (BB4CMIP) for biomass burning emissions (van Marle et al., 2017). In addition, natural sources of NMVOCs, NO_x and CO were taken from Precursors of Ozone and their Effects in the Troposphere inventory (POET, Granier et al. (2005)) following Naik et al. (2013), except for isoprene and monoterpene emissions which are calculated online as described in Horowitz et al. (2020) and Rasmussen et al. (2012). As described in Horowitz et al. (2020), lightning NO_x emissions are calculated interactively as a function of subgrid convection, as diagnosed by the double plume convection scheme described by Zhao et al. (2018). The lightning NO_x source is calculated as a function of convective cloud-top height, following the parameterization of Price et al. (1997), and is injected with the vertical distribution of Pickering et al. (1998). Well-mixed greenhouse gas concentrations are specified following Meinshausen et al. (2017). In particular, atmospheric concentrations of ODS, including CFC-11, CFC-12, CFC-113, and HCFC-22, and CH_4 concentrations are specified at the surface as a global mean lower boundary condition, with concentrations beyond the surface subsequently determined by various chemical and dynamical processes. A summary of historical CO emissions, CH_4 concentrations and NO_x emissions are shown in Fig. 1.

2.2 Model Runs

We conducted model integrations from 1980-2014, using an initialisation state from an GFDL AM4.1 historical run. In addition to a 'Base' run which includes the time-varying historical emissions of the various species as per Horowitz et al. (2020), we conducted 'all-but-one' runs where we investigate the effects of various emitted species which could affect OH concentrations, namely: NO_x; CH_4; CO; NMVOC; and ozone-depleting substances ('ODS'). These runs are configured so as to systematically fix the emissions of a particular species to 1980 values in order to isolate the effects of each individual species by comparing with the 'Base' run. Additionally, we include a run where all the above species are set to 1980 values ('Met'), which allows us to diagnose the effects of meteorology. Note that, as lightning NO_x emissions as well as biogenic terpene and isoprene
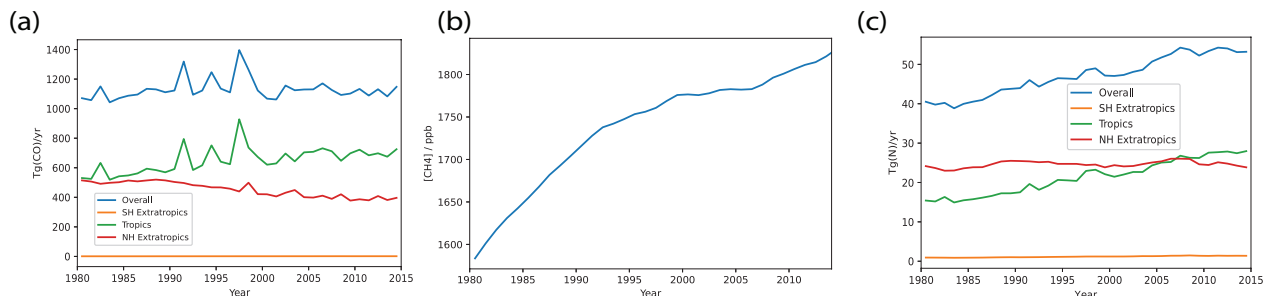
Figure 1. Historical time series of (a) regional CO emissions, (b) CH_4 surface concentrations, and (c) regional NO_x emissions used for this study. The Southern Hemisphere (SH) extratropics is defined as $90^{\circ}S - 30^{\circ}S$, the Tropics as $30^{\circ}S - 30^{\circ}N$, and the Northern Hemisphere (NH) extratropics as $30^{\circ}N - 90^{\circ}N$. Globally, CH_4 concentrations have inceased by $\sim 16\%$. Non-lightning NO_x emissions have also increased by $\sim 30\%$ globally over this period, with this increase driven by the Tropics. CO emissions see IAV but little trend globally over this period, but do see a decreasing trend in the NH extratropics offset by an increasing trend in the Tropics.

emissions are interactively-calculated, their impacts are included in the 'Met' run. The 'NO_x' run only fixes non-lightning NO_x emissions at 1980 levels, and the 'NMVOC' run only fixes the emissions of other NMVOCs than biogenic terpene and isoprene.

While the 'Base' and 'Met' run will be analyzed on their own, for the sensitivity runs involving each emission driver, $i = NO_x$, CH_4, CO, VOC, ODS, for each quantity analysed, e.g. tropospheric airmass-weighted OH concentrations, we calculate a derived quantity as per Eq. 2. Quantity_i will be the quantity if the emission driver i was set to 1980 values, but everything else (other drivers and meteorology) was as per the 'Base' run, so taking the difference $(\text{Quantity}_{\text{Base}} - \text{Quantity}_i)$ allows us to isolate the impact of driver i, with respect to the 1980 value from the 'Base' run $(\text{Quantity}_{\text{Base,1980}})$ and removes the impact of meteorology and other drivers. Adding the anomaly to the 1980 value from the 'Base' run then allows us to diagnose the impact that the emission driver i would have on the quantity in isolation.

$$\text{Quantity}_{i,\text{derived}} = (\text{Quantity}_{\text{Base}} - \text{Quantity}_i) + \text{Quantity}_{\text{Base,1980}} \tag{2}$$

In the original run, Quantity_i shows a negative deviation from $\text{Quantity}_{\text{Base}}$, and also shows some variability as a result of other factors like meteorology, the derived quantity, $Quantity_{i,derived}$, would show a positive deviation from $\text{Quantity}_{\text{Base}}$ instead, in addition to having the variability from other factors like meteorology removed.

2.3 Chemical Budget Term Analysis

To complement our analysis of the main potential drivers of [OH] from 1980 to 2014, we provide a bottom-up, mechanistic understanding of how the various drivers affect [OH], by looking at the chemical budget. As described in Eq. 1, changes in [OH] can be traced to changes in the OH chemical production and loss terms. We follow the methodology of Lelieveld et al. (2016) to analyse the chemical budget terms. We group the production terms into: primary production (Reactions R1-R2);

secondary production, or recycling, via NO_x (Reaction R3); secondary production via O_3 (Reaction R4); secondary production via H_2O_2 photolysis (Reaction R5); and other OH production reactions (e.g. from recyling from peroxy radicals via Reaction R13 or other photolysis reactions.) Meanwhile, the loss terms are grouped into: loss via CO from Reaction R6; loss via CH_4 from Reaction R7; loss via NMVOC from Reaction R7; loss via NO_y, which includes loss via Reaction R11 but also via

165   other nitrogen-containing species like HNO_3, NH_3 and nitrogen-containing isoprene oxidation products; loss via HO_y, which includes loss via H_2, O, O_3, H_2O_2, HO_2 and also self-reaction; and other loss reactions, which include loss to sulphur- and halogen-containing species.

2.4   Evaluation of Modelled CO and NO_x

We identified CO, non-lightning NO_x emissions and CH_4 as key drivers of [OH] from 1980 to 2014, of which CH_4 concen-
170   trations are prescribed in the model, so it is important to look at how well the modelled CO and NO_x compare to observations. This would allow us to say to what extent our findings from our model study could be generalised to the real world.

2.4.1   Comparison of Modelled CO column with Measurements of Pollution in The Troposphere (MOPITT) Satellite Observations

We evaluate the modelled tropospheric CO column trends against those measured by the MOPITT instrument, following
175   Horowitz et al. (2020). The MOPITT V8 Joint (NIR+TIR) retrievals (Deeter et al., 2019) during 2001-2014 are used, which are available from the NASA Earthdata archive (https://earthdata.nasa.gov). The modelled CO column is interpolated to the same grid as the monthly MOPITT observations, and the averaging kernel is applied to the modelled monthly mean CO profiles following documentation provided by Deeter (2003) in order to compare between modelled and observed MOPITT CO columns.

180   Horowitz et al. (2020) previously calculated the seasonal climatological mean CO column in the GFDL AM4.1 and found a persistent model CO column low bias in the NH and high bias in the SH compared to MOPITT observations across seasons. Horowitz et al. (2020) also compared modelled surface CO concentration with measurements from a globally distributed network of air sampling sites maintained by the Global Monitoring Division (GMD) of the Earth System Research Laboratory at the National Oceanic and Atmospheric Administration (NOAA) (Pétron et al., 2019; data available at ftp://aftp.cmdl.noaa.
185   gov/data/trace_gases/co/flask/) and the NH low bias/SH high bias was also seen in remote site comparisons. In this study, we complement the analysis by comparing the annual mean CO column trends. We also look at the global (60^oS-60^oN) area-weighted 12-month rolling mean CO columns to compare IAV.

2.4.2   Comparison of Modelled Tropospheric NO_2 column with Ozone Monitoring Instrument (OMI) Satellite Observations

190   We also identified NO_x trends as driving the modelled increase in [OH], so it would be useful to find out if the NO_x trends modelled matched well with observations. Compared to CO which has a lifetime of about a month, NO_x has a relatively shorter

tropospheric lifetime of $\sim$ day (Jacob, 2000), and so NO_x burden is much more concentrated near emission areas. Therefore, an evaluation of tropospheric NO_x observations will more readily give information about emissions and how they change with time. We analyse the NO_2 column trends from 2005 to 2014 to coincide with when OMI observations started, noting that the shorter time period may limit the trend analysis.

We use the OMI v4 data (Lamsal et al., 2021) that has been processed into a gridded dataset by Goldberg et al. (2021). The gridded data do not come with information necessary to calculate the averaging kernel, which, as discussed earlier, is necessary for a better comparison between retrievals and modelled quantities. In particular, for UV-visible measurements such as OMI, the tropospheric retrievals of NO_2 can be heavily influenced by aspects such as clouds, surface albedo, the presence of a stratospheric background and aerosols, as well as the assumed a priori vertical profile (Eskes and Boersma, 2003), resulting in potentially large errors. The Differential Optical Absorption Spectroscopy (DOAS) technique used is sensitive to the a priori vertical profile, and using the averaging kernels allows for the model-to-satellite comparisons to not be affected by systematic biases introduced by the a priori assumptions. This work will not use averaging kernels, and thus the comparisons between the model and OMI observations are only an approximation. We furthermore also note that the tropopause level used for processing the model data, which we determined using the WMO definition, is also different from that used in the OMI data. These factors add to the qualitative nature of the comparisons between the model and OMI observations done in this study. However, despite these approximations, the purpose of this analysis is to show consistency between input NO_x emission trends, modelled NO_x trends, and observed trends.

3 Results

3.1 Tropospheric [OH] Trends from 1980 to 2014

As seen in Fig. 2(a), tropospheric airmass-weighted [OH] has increased by $\sim 5\%$ from 1980 to 2014 in the Base simulation. The 1980-2014 period fits a linear trend of 0.033 ± 0.06 molec cm^{-3}yr^{-1} (95% Confidence Interval (CI)) as seen from Fig. 2(d) and exhibits some IAV throughout the period. The simulated increase is well within the range found in Zhao et al. (2019) and on the upper bound of the range found in Naik et al. (2013). In terms of the anomaly with respect to 1998-2007 mean modelled $\sim 10\%$ agrees well with that simulated in ESMs participating in CMIP6 using the same emission drivers (Stevenson et al., 2020). In detail, we see that the 1980-2010 period is dominated by an increasing trend. From 2010 to 2014, we see a slight decrease; however, as shown by He et al. (2020), looking further into 2015-2017, [OH] increases again, suggesting that the overall increasing trend is robust. The increase, especially in the period 2000-2010, is in contrast to some observational studies like Rigby et al. (2017) and Turner et al. (2017) who found a decrease instead. The increase over the 35-year period 1980 to 2014 is also in contrast to the period from 1870 to 1980, where [OH] did not exhibit a trend (Stevenson et al., 2020; Szopa et al., 2021). As seen in Fig. 2(b), the increase in [OH] occurs throughout the depth of the troposphere, but with the largest increase seen from the surface to the lower troposphere. This could suggest that the increasing [OH] trend is driven by mainly surface drivers rather than, for example, lightning NO_x emissions.

Next, we look at the sensitivity of simulated [OH] to various chemical drivers of [OH]. The simulated global tropospheric airmass-weighted [OH] are plotted in Fig. 2(c), with the individual model runs analysed as per Section 2.2. As seen in Fig. 2(d), the increasing non-lightning NO_x emissions caused the largest positive [OH] trend of 0.041 ± 0.004 molec cm^{-3}yr^{-1} (95% CI), while there is a small positive trend arising from decreasing ODS concentrations of 0.005 ± 0.0015 molec cm^{-3}yr^{-1} (95% CI). This suggests that the increasing non-lightning NO_x emissions of $\sim 30\%$ (Fig. 1(c)) have been the largest driving force behind the overall [OH] increase. However, the 'NO$_x$' run overestimates the positive trend and fails to capture some of the modelled features in the 'Base' run, suggesting the important contributions of other factors which dampen the effect of increasing non-lightning NO_x as we discuss below.

In terms of factors that contribute negatively to the [OH] trend, increasing CH_4 concentrations caused the largest negative trend of -0.012 ± 0.02 molec cm^{-3}yr^{-1} (95% CI), and there is also a small negative trend simulated in the 'NMVOC' run of -0.003 ± 0.02 molec cm^{-3}yr^{-1} (95% CI). The 'CH$_4$' run simulates a roughly 4% decrease from 1980 to 2014 as seen in Fig. 2(c), consistent with the increasing CH_4 concentrations seen over the period. We see that [OH] decreases from 1980 to 2000 before stabilizing up to 2007 after which it resumes its decrease. This follows the CH_4 trend, plotted in Fig. 1(b), seen over this period, where CH_4 has increased from 1980 to 2000 before stabilizing up to 2007 after which it resumed its increase, such that the CH_4 burden has increased by about 16% by 2014 compared to 1980 values. Over the 1980-2014 period, CO emissions do not contribute to the global average OH trend but induce large IAV (see section 3.3) as evident in the CO simulation. This lack of OH trend is attributed to the lack of trend in CO emissions over the 35 year period as seen in 1(a).

With NO_x and CH_4 identified as the main factors affecting the global [OH] trend, we conducted an additional sensitivity run accounting for their combined effects ('CH$_4$ + NO$_x$'). As seen in Fig. 2(d), the resultant OH trend of 0.032 ± 0.05 molec cm^{-3}yr^{-1} (95% CI) matches the 'Base' run well, suggesting that the combined effects of CH_4 and NO_x drive the overall modelled [OH] trend.

Other factors, such as meteorology, that have been known to drive [OH] do not show up strongly on the global tropospheric mean analysis. This result is consistent with He et al. (2021), who used AM4.1 driven by the same emissions as this study but varied the meteorology field (model-calculated, the National Centers for Environmental Prediction (NCEP) reanalysis and Modern-Era Retrospective analysis for Research and Applications, Version 2 (MERRA-2) meteorology), and found that meteorology could affect the magnitudes of mean [OH], but not the trend. Nonetheless, these other factors could have important regional contributions, which we explore in the next section.

3.2 Regional Tropospheric [OH] Trends from 1980 to 2014

Next, we analyze the spatial patterns of the [OH] trends in order to get a more nuanced view of how [OH] is changing. In the 'Base' run, the tropospheric airmass-weighted column mean [OH] increases over most areas, with the largest increases over much of Tropical Asia as well as China (Fig. 3). On the other hand, there are also areas such as over USA, some parts of Western Europe and Northern Russia, where there is a small decreasing trend, as well as Central Africa which sees a pronounced decreasing trend.
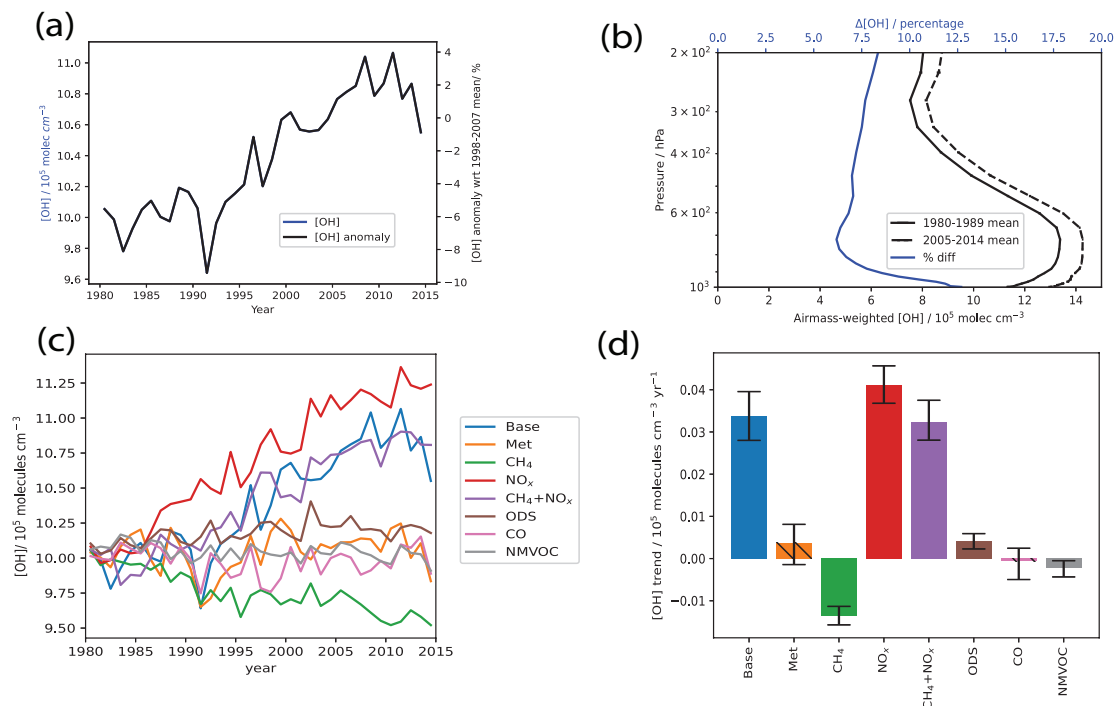
Figure 2. Tropospheric airmass-weighted [OH] (a) time series for the 'Base' run as well as the anomaly with respect to the 1998-2007 mean from 1980 to 2014; (b) 10-year global area-weighted airmass-weighted mean [OH] at various altitudes for 1980-1989 (black solid line) and 2005-2014 (black dotted line), and the percentage [OH] difference at each altitude (blue line); (c) tropospheric airmass-weighted [OH] time series and (d) trends from the Base simulation and from the sensitivity simulations with all ('Met') and individual short-lived emissions held constant at 1980 levels. For (b), error bars for the 1980-1989 and 2005-2014 means represent ± 1 standard deviation about the 10-year mean at each pressure level. For (d), trends are calculated using the Theil-Sen method, and error bars show the 95% confidence interval. Bars are hashed when no significant trend is detected at the 95% level using the Mann-Kendall test. From (a), tropospheric airmass-weighted [OH] has increased by $\sim 5\%$ from 1980 to 2014 in the Base simulation. As seen in (b), the increase in [OH] occurs throughout the depth of the troposphere, but with the largest increase seen from the surface to the lower troposphere, and this could suggest that the increasing [OH] trend is driven by mainly surface drivers. From (c) and (d), we see that globally the [OH] increasing trend is driven by the combined effects of CH_4 and NO_x.

We next see that the [OH] changes in the 'NO$_x$' run are positively correlated with the changes in non-lightning NO$_x$ emissions (Fig. 4(a)), and itself matches the 'Base' run changes very well. This reinforces the earlier result that non-lightning NO$_x$ emissions have been the main driver behind the modelled [OH] trend. However, non-lightning NO$_x$ emissions alone seem to overpredict the decreasing trends over Western Europe and Northern Russia and increasing trends in the other regions. The addition of the CH_4 trend does not change the spatial pattern much, since [CH_4] increases uniformly across the surface, but it helps to bring the positive trends in line with 'Base'. However, this then leads to a larger overprediction of the decreasing trends over Western Europe and Northern Russia.

This, in turn, is largely rectified by including the effects of CO emissions. We see that the 'CO' run produces changes in [OH] that are negatively correlated with the changes in CO emissions (Fig 4(b)), in particular an increasing trend in [OH] over USA, Europe and Russia associated with declining CO emissions. The addition of these effects therefore helps to dampen the effects of declining NO_x emissions and increasing CH_4 concentrations in those regions. The dampening effect of CO on NO_x effects in these particular regions is due to the large spatial correlation between the NO_x and CO emission trends as seen in Fig. 4(a) and (b).

The large negative trend over Central Africa results not only from contributions from increasing CH_4 concentrations and increasing NMVOC emissions (Fig. 4(c)), which tend to reduce [OH] by increasing chemical loss, but also from meteorology-related factors.

In terms of meteorology-related factors, trends in lightning NO_x have been suggested to contribute to [OH] trends (e.g. He et al., 2020; Fiore et al., 2006). From Fig. 4(d), Our meteorology-driven simulation did not show significant lightning NO_x trends except for a significant negative trend over Central Africa, which could further help explain the locally negative [OH] trend. Looking at other factors that could affect [OH], we see from Fig. 4(e) that isoprene emissions, which are interactively calculated in our model, have increased in specific regions in the meteorology-driven run, such as over the Amazon, Eastern USA, Central Africa, and parts of Asia such as Eastern China. Indeed, we see that these regions are associated with negative [OH] trends in the meteorology-driven run, with Central Africa seeing a particularly large effect. We also see, from Fig. 4(f) that, in the meteorology-driven run, the water vapor burden has increased sigificantly in most regions, which tends to locally increase OH chemical production. These competing local effects on [OH] from meteorology-driven factors accounts for the absence of a globally-averaged [OH] trend contribution from meteorology.

Overall, this analysis reinforces the findings from the global average analysis of the key role of non-lightning NO_x emissions in driving the overall [OH] trends, modulated by the changes in CH_4 concentrations. However, the regional trends highlight the additional importance of CO emissions, especially in regions in the extratropical NH, as well as the importance of increasing NMVOC emissions and meteorology-driven decreases in lightning NO_x as well as increases in isoprene emissions in explaining the negative [OH] trend over Central Africa. Our findings from the spatial column tropospheric analysis also hold when we looked at particular pressure levels in the surface as well as the middle and upper troposphere (see Fig. S1 of the Supplementary Material).

3.3 Interannual Variability

In the above analyses, we found that, in general, CH_4 and NO_x effects can largely explain the long-term [OH] trend over 1980-2014. However, the combined effects of CH_4 and NO_x alone do not account for the short-term variability in [OH] seen over this period. In particular, there are some features such as the dip in 1992 as well as the dips and spikes seen between 1995 to 2000 that the 'CH_4+NO_x' run misses. As seen in Fig. 5, in the global average there is a year-on-year change of up to about $0.4 \, \mathrm{molec \, cm^{-3} yr^{-1}}$, with 13 out of the 34 years after 1980, or about one-third of the years, showing a negative year-on-year change.
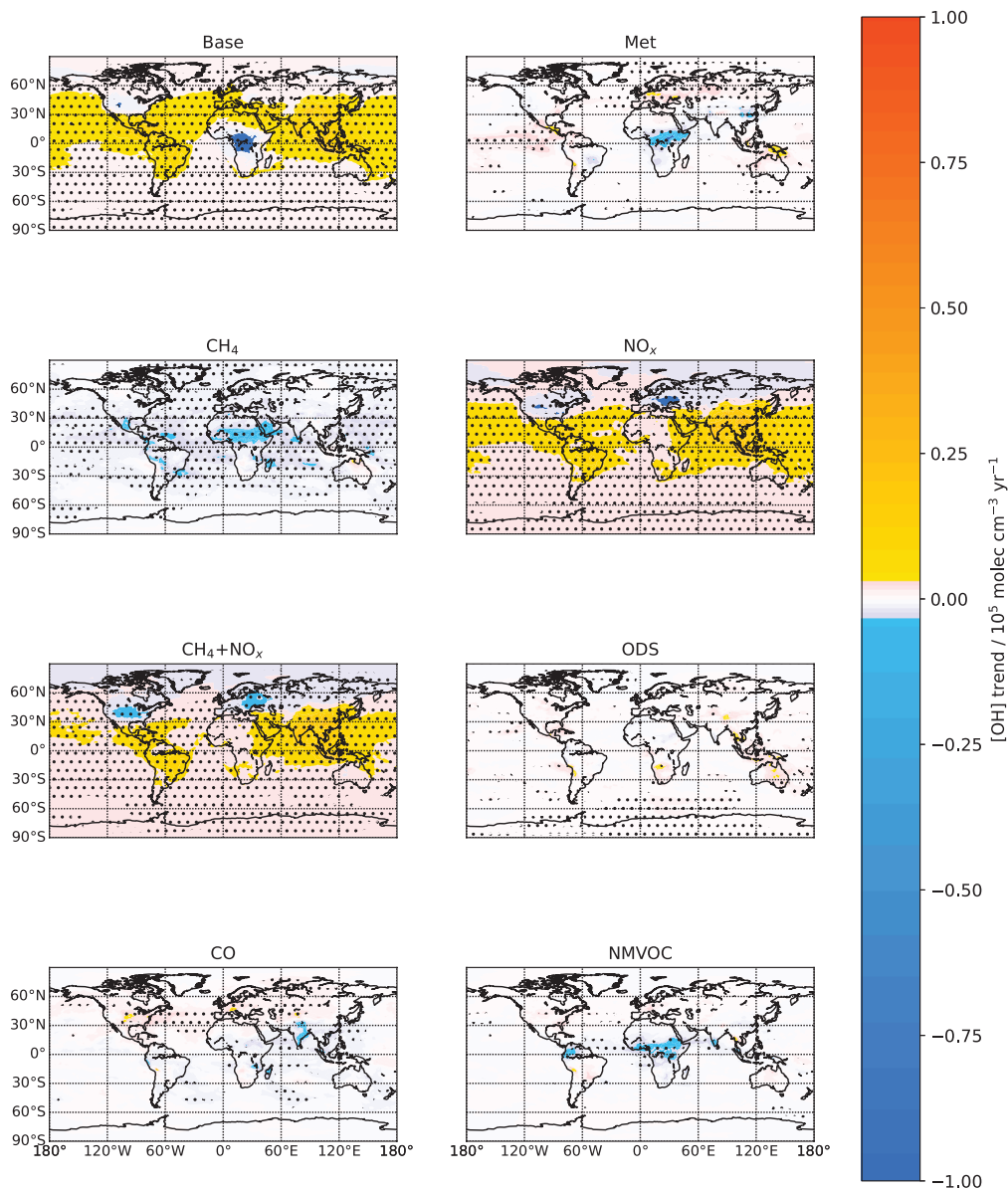
Figure 3. Trends in tropospheric airmass-weighted OH concentrations by grid box from 1980 to 2014 for the different model runs. Trends are calculated using the Theil-Sen method. Stipples show areas where a significant trend is detected at the 95% level using the Mann-Kendall test. In the 'Base' run, the tropospheric airmass-weighted column mean [OH] increases over most areas, with the largest increases over much of Tropical Asia as well as China. These increases are also largely driven by the combined effects of non-lightning NO_x emissions and CH_4 concentrations. On the other hand, there are also areas such as over USA, some parts of Western Europe and Northern Russia, where there is a small decreasing trend, as well as Central Africa which sees a pronounced decreasing trend.
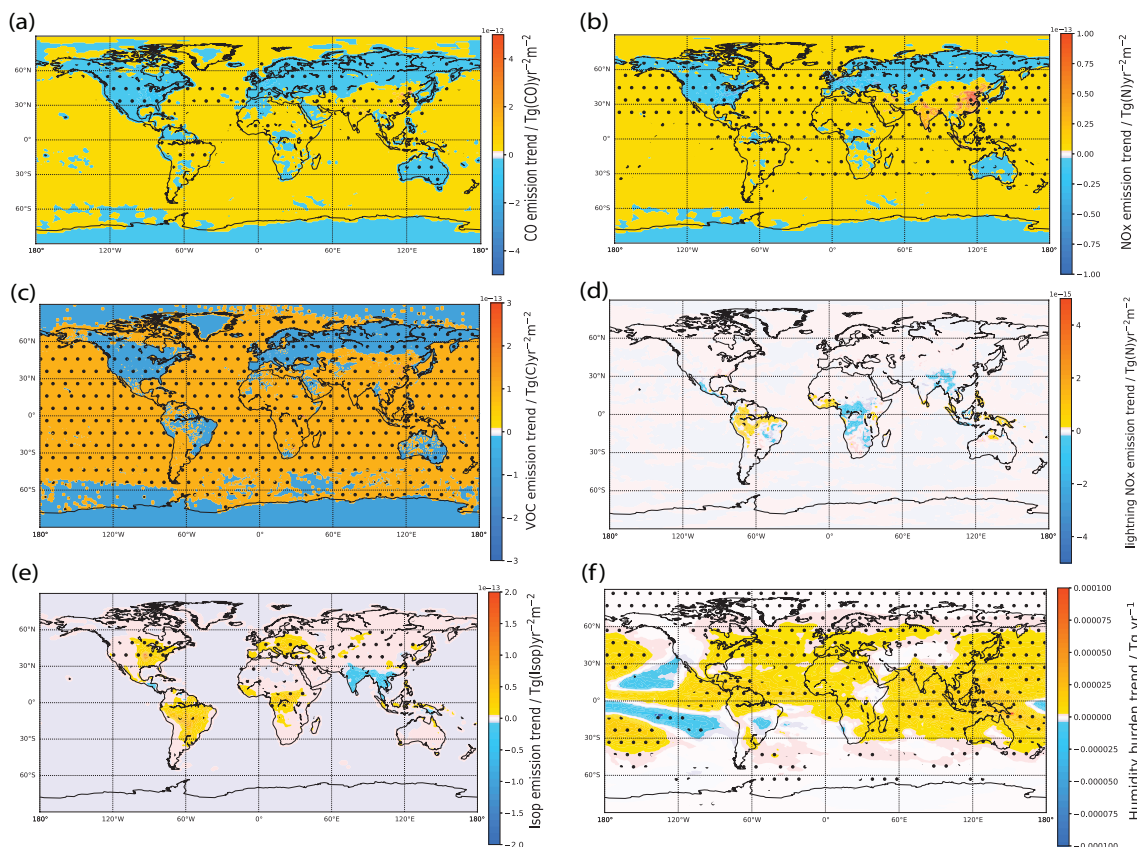
Figure 4. Spatial trends of (a) non-lightning NO_x, (b) CO, (c) NMVOC, (d) lightning NO_x (e) biogenic isoprene emissions, and (f) humidity from 1980-2014. Trends and stippling are as per Fig. 3, except for (a) and (b) and (d), where we additionally remove stippling when the trend is below 10^{-16} Tg/yr^{-2}m^{-2}. [OH] changes in the 'NO$_x$' run are positively correlated with the changes in non-lightning NO$_x$ emissions (seen in (a)) and itself matches the 'Base' run changes very well. Meanwhile, the 'CO' run produces changes in [OH] that are negatively correlated with the changes in CO emissions (seen in (b)). The large negative trend over Central Africa results not only from contributions from increasing CH$_4$ concentrations and increasing NMVOC emissions (seen in (c)), which tend to reduce [OH] by increasing chemical loss, but also from meteorology-related factors, such as lightning NO$_x$ as seen in (d), isoprene emissions as seen in (e). From (f), we see the water vapor burden has increased sigificantly in most regions, which tends to locally increase OH chemical production. These competing local effects on [OH] from meteorology-driven factors accounts for the absence of a globally-averaged [OH] trend contribution from meteorology.

We see from Fig. 2(c) that the 'Base' and meteorology-driven runs are positively correlated, with a Pearson correlation coefficient of $r = 0.82$. As summarized in Section 1, meteorology can affect [OH] in various ways. We further see also that the 'CO' run (pink line) also exhibits variability features that are also seen in the 'Base' run. This could be related to variability in
300 biomass burning, as pointed out by Holmes et al. (2013).
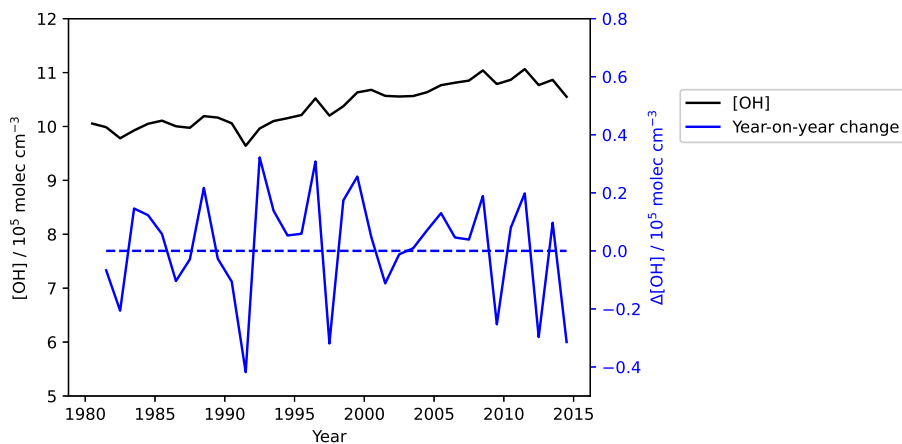
Figure 5. Base OH Concentrations plotted on the lefthand axis (black), and Year-on-Year changes plotted on the righthand axis (blue). In the global average there is a year-on-year change of up to about $0.4 \; \mathrm{molec \; cm^{-3} yr^{-1}}$, with 13 out the 34 years after 1980, or about one-third of the years, showing a negative year-on-year change. The global IAV is driven by IAV in meteorology-related factors and CO emissions.

3.4 OH production and loss terms

3.4.1 Chemical Budget Terms in Base Run

We first look at how the proportions of each of the production and loss terms evolves with time from 1980 to 2014 in the 'Base' run, as shown in Fig. 6(a) and (b). Firstly, we see that the relative proportions stay roughly constant throughout the time period,
305   suggesting that all of the reaction terms have increased in tandem with the total. In terms of the biggest changes, we see that, for OH production terms, the primary production term has increased in proportion by the largest amount (+0.5%), followed by small increases in the NO_x and O_3 recycling reactions (0.1% each) at the expense of the other two terms. Meanwhile for the OH loss terms, the CO loss reaction sees quite large variability, especially from 1990 to 2000, and decreases by 1.1% overall. The CH_4 loss reaction increases by 0.9% overall. Comparing the production values with Table 1 of Lelieveld et al. (2016),
310   the percentages are roughly consistent. However, our model seems to have a larger proportion of primary production (42%) compared to Lelieveld et al. (2016) (33%). Looking at the loss reactions, we have a lower proportion of NMVOC loss (20% compared to 29%), and also a higher loss to HO_y (25% compared to 18%).

     We next look at the chemical budget terms in the 'Base' model run. From Fig. 6(c), we see that global tropospheric airmass-weighted OH production and loss match closely with one another, consistent with the pseudo steady-state assumption. Both
315   have increased by about 14% by 2014 compared to 1980, showing a clear trend. We also see some IAV throughout the period, with year-on-year changes of up to 2%. Relating these results to the earlier findings, where we saw an increasing [OH] trend, the increasing trend in both production and loss (as they balance each other in steady-state) should therefore be driven by an increasing trend in production, and that in turn should be associated with the net NO_x and CH_4 effects. Meanwhile, the IAV observed in the OH concentrations should also be associated with the IAV seen in the production and loss, and this in turn
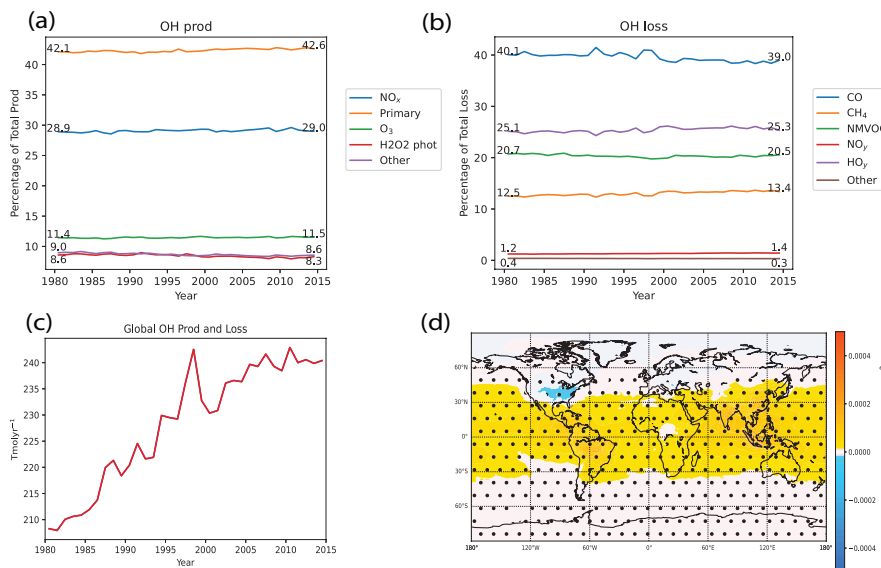
Figure 6. Tropospheric Airmass-weighted OH chemical production and loss terms in the 'Base' run. (a) Evolution of the proportion of each production reaction with respect to the total, and (b) Same but for loss reactions instead. (c) Time evolution of global total production and loss terms (curves overlap because OH is in pseudo steady-state.) (d) Spatial airmass-weighted tropospheric OH chemical production trend over the 1980-2014 period, with stippling and trends as per Fig. 3. From (a) and (b), we see that the relative proportions stay roughly constant throughout the time period, suggesting that all of the reaction terms have increased in tandem with the total, and the values are roughly consistent with Table 1 of Lelieveld et al. (2016). From (c), both global tropospheric airmass-weighted OH production and loss have increased by about 14% by 2014 compared to 1980, showing a clear trend. We also see some IAV throughout the period, with year-on-year changes of up to 2%. Relating these results to the earlier findings, where we saw an increasing [OH] trend, the increasing trend in both production and loss (as they balance each other in steady-state) should therefore be driven by an increasing trend in production, and that in turn should be associated with the net NO_x and CH_4 effects. Meanwhile, the IAV observed in the OH concentrations should also be associated with the IAV seen in the production and loss, and this in turn should be affected by meteorological factors, factors that are driven by meteorology like lightning NO_x and biogenic VOC emissions, and CO emissions. From (d), we see that spatial chemical production trends matches the spatial [OH] trend plot for the 'Base' run in Fig. 3, suggesting again the role of chemical production (and loss) in driving [OH] trends.

320   should be affected by meteorological factors, factors that are driven by meteorology like lightning NO_x and biogenic VOC emissions, and CO emissions. We delve into these hypotheses further in the following subsections when we do a sensitivity analysis for the budget terms.

Lastly, Fig. 6(d) shows the spatial plot of OH production trends from 1980 to 2014 for the 'Base' run. We see that it matches the spatial [OH] trend plot for the 'Base' run in Fig. 3, suggesting again the role of chemical production (and loss) in driving
325   [OH] trends.

3.4.2 Chemical Budget Term Sensitivity Analysis

We next look at how these budget terms are affected by the input emissions by doing a sensitivity analysis using our model runs, by analyzing the sensitivity simulations involving each emissions driver as well as the meteorology-driven simulation. We focus our attention on the major terms represented in the budget. For production terms, we look at the primary production as well as secondary production via NO_x and O_3, together accounting for $\sim 84\%$ of total production. For loss terms, we focus on loss via CO, HO_y and CH_4, accounting for $\sim 78\%$ of total loss. Unfortunately, we did not have enough model diagnostics to study loss to NMVOCs, and this is left as potential future work. From the earlier analyses, the NMVOC-related budget term is unlikely to play a large role in affecting the global [OH] trend, even though it may have a regional role. Also, while analysing the changes in these budget terms, we note that, due to the fact that [OH] is in pseudo steady-state, we will always have total production and loss approximately balancing at all times. This means that a change in production can precede a change in loss, or vice versa. To disentangle the effects, we have to rely on our physical understanding of the underlying chemistry, and can take cues from how [OH] itself is changing.

Since our analysis in section 3.1 showed the dominant role of NO_x in driving [OH] increases over the 1980-2014 period, we focus here on NO_x. From Fig. 7 (c), we see from the red line that increasing NO_x emissions have led to an increase in OH reycling from NO_x. This is to be expected, as the increasing NO_x emissions as seen in Fig. 1(c) drive an increase in the tropospheric NO_x burden (see Fig. S2(a) of the Supplementary Material). This therefore increases the NO_x reaction recycling rate from Reaction R3, acting to increase the partitioning of HO_x into OH. NO_x emissions have also caused an increase in the other major production terms. We can understand this via the impact of NO_x emissions on tropospheric O_3. Increases in NO_x emissions have driven the increasing trend seen in tropospheric O_3 burden (see Fig. S2(b) of the Supplementary Material), with the increase of $\sim 30\%$ of non-lightning NO_x emissions leading to a $\sim 10\%$ increase in O_3. This suggests that the atmosphere as a whole is NO_x-limited with respect to ozone production, with ozone production occuring via Reactions R8 - R10. This is consistent with other studies e.g. Lawrence et al. (2003) who found that the lofting of surface NO_x drove significant increases in O_3 production over the tropospheric column. The increasing O_3 concentrations lead to an increase in primary production via Reactions R1 - R2. The increasing O_3 concentrations also lead to enhanced OH recycling via O_3 through Reaction R4, which further partitions HO_x into OH. Murray et al. (2013) previously found that lightning NO_x influenced both primary and secondary production, and we show here that non-lightning surface NO_x emissions also have the same effect in our model. The increased OH production as a result of NO_x emissions then leads to an increase in [OH]. As loss fluxes are proportional to [OH], this in turn then leads to increased OH losses (as seen in Fig. 7 (b), (d) and (f)), eventually keeping OH in pseudo steady-state.

Next, we look at the impacts of CH_4, which we found to suppress the increasing [OH] trend. We first see the primary effect of increased CH_4 in depleting OH in Fig. 7(f). Furthermore, oxidation of CH_4 via Reaction R7 eventually leads to the production of CO (see Fig. S2(c) of the Supplementary Material), which then leads to a small increase in OH loss via CO in Fig.7(b). However, as CH_4 is a tropospheric ozone precursor, such as via Reaction R8 - R10, the increase in CH_4 also leads to increased tropospheric O_3 (see Fig. S2(b) of the Supplementary Material), thereby slightly enhancing primary production and

360   OH recycling via O_3 as well. Hence, this could explain why the overall net negative effect of CH_4 on [OH], which includes a mixture of enhanced losses and production, is smaller. Furthermore, we see in Fig. 7(f) that the NO_x run also contributes roughly equally to the OH loss due to chemical reaction with CH_4, and this further highlights the importance of changes in OH production associated with NO_x.

     Lastly we look at the impacts of CO, which we found to have a regional effect on the [OH] trend. As identified earlier in Fig.

365   3, the main region where CO emissions have affected the [OH] trend is in some regions in the extratropical NH, such as Eastern USA and Western Europe, where a decrease in CO emissions led to an increase in [OH], and in South Asia and East China, where an increase in CO emissions led to a decrease in [OH]. As seen for the 'CO' run in Fig. 8, regions of decreasing CO emissions see decreasing OH loss via reaction with CO and hence an increase in [OH], and vice versa. However, comparing the 'Base' and 'NO_x' runs, we also see that the base OH loss flux to CO is also driven by the [OH] changes associated with

370   the 'NO_x' run, and this again highlights the importance of changes in OH production associated with NO_x.

     Additionally, we find that meteorology plays an important role for IAV in OH primary production, while CO emissions are more important for IAV in the OH loss flux to CO. The former is evident from Fig. 9 which shows that OH primary production is strongly correlated with changes in specific humidity (q) (Pearson correlation coefficient $r = 0.90$) which itself is strongly correlated with temperature (r = 0.96). For the latter, as seen in Fig. 10(a), CO emissions are positively correlated with OH

375   loss to CO in the 'Base' run ($r = 0.69$). This thereafter drives overall IAV in total loss and production. As seen in Fig. 10(b), where we plot the year-on-year changes in [OH] on the lefthand axis (black), as well as the year-on-year changes in total OH production and loss and that of the OH loss to CO on the righthand axis (blue), we first notice that the OH year-on-year production/loss change (solid blue) is highly correlated with that of the OH loss to CO (dotted blue) with Pearson correlation coefficient $r = 0.94$, suggesting that the OH loss to CO is indeed driving the IAV seen in total production/loss. The year-on-year

380   change in production/loss, in turn, is anti-correlated with the year-on-year change in OH, with Pearson correlation coefficient $r = -0.36$.

4   Evaluation of Modelled CO and NO_x

4.1   CO: Comparison with Satellite Column and In Situ Surface Measurements

Fig. 11(a) shows the MOPITT and modelled CO column trends from 2001 to 2014, and Fig. 11(b) shows the input CO emission

385   trends over the same time period. The MOPITT CO column generally sees significant negative trends throughout the spatial domain, consistent with results from Yin et al. (2015). However, the modelled CO columns show significant positive trends above China and India with weaker positive trends in parts of Africa and the Middle-East and negative trends over most other parts of the world. The mixed modelled CO column trends mirror the CO emission trends, especially the increasing trend over China and South Asia, and are in poor agreement with trends derived from MOPITT. The MOPITT and modelled

390   CO column trends thus show a poor agreement. Comparing Fig. 11(a) and (b), we see that the modelled CO column trends exhibit a high spatial correlation with the input CO emission trends, and so the mismatch between observed and modelled CO column trends could point towards some deficiencies in the input emissions, which drive the high bias in CO column trends
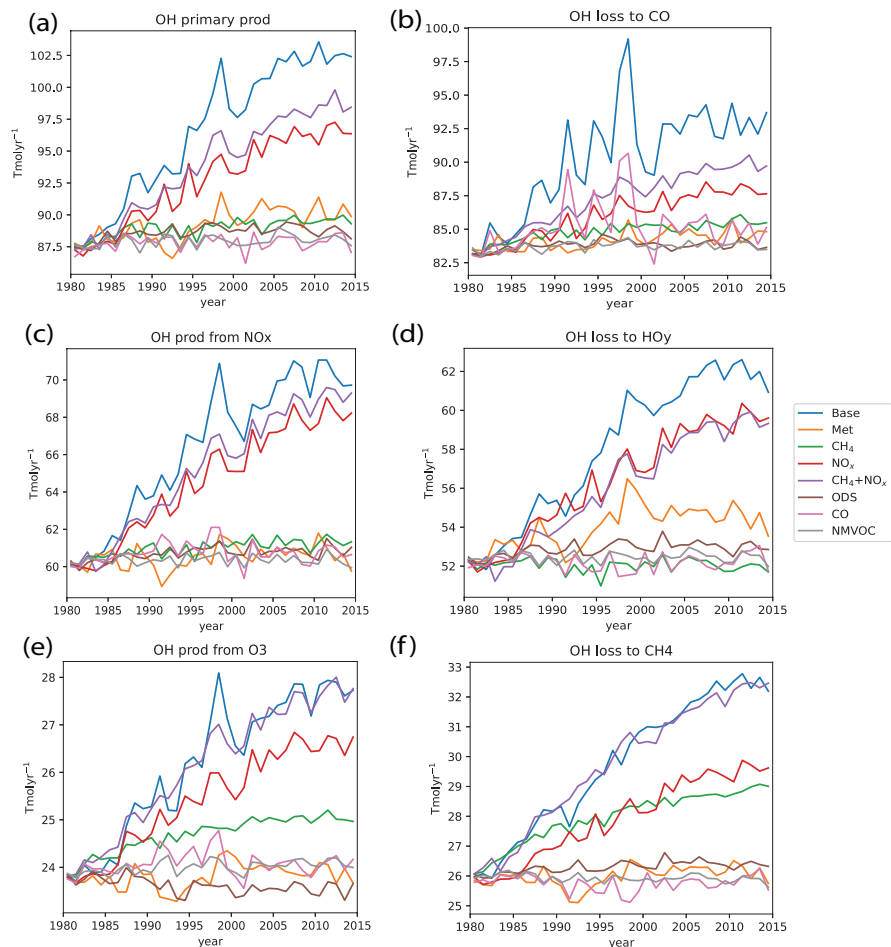
Figure 7. OH chemical production and loss budget terms for the different model runs. (a), (c) and (e) show the production terms, accounting for $\sim 84\%$ of total OH production. (b), (d) and (f) show the loss terms, and account for $\sim 78\%$ of total OH loss. Globally, increasing NO_x emissions have led to increasing primary and secondary OH production, while increasing CH_4 concentrations have led to increased OH loss via reaction with CH_4 that is offset by increased secondary OH production due to the increase in tropospheric O_3.

over China and South Asia and in turn leads to the general high bias globally due to transport from these regions especially via the prevailing Westerlies (Zheng et al., 2018). Zheng et al. (2019) suggest that emissions from the version of CEDS used

395 in our study are inconsistent for China and South Asia. Whereas the version of CEDS used in this study (and other CMIP6 runs) suggests rapidly increasing anthropogenic CO emissions from China and South Asia, Zheng et al. (2019) found instead a decreasing trend for China and a modestly-increasing one for South Asia. Elguindi et al. (2020) compared regional bottom-up inventories, global bottom-up inventories which include CEDS, and top-down estimates, and they also found that CEDS (and other global bottom-up inventories) showed an increasing trend that was larger than seen in regional inventories and top-down

400 emissions. They further point out that, for these countries which are experiencing rapid changes in their economies, technology
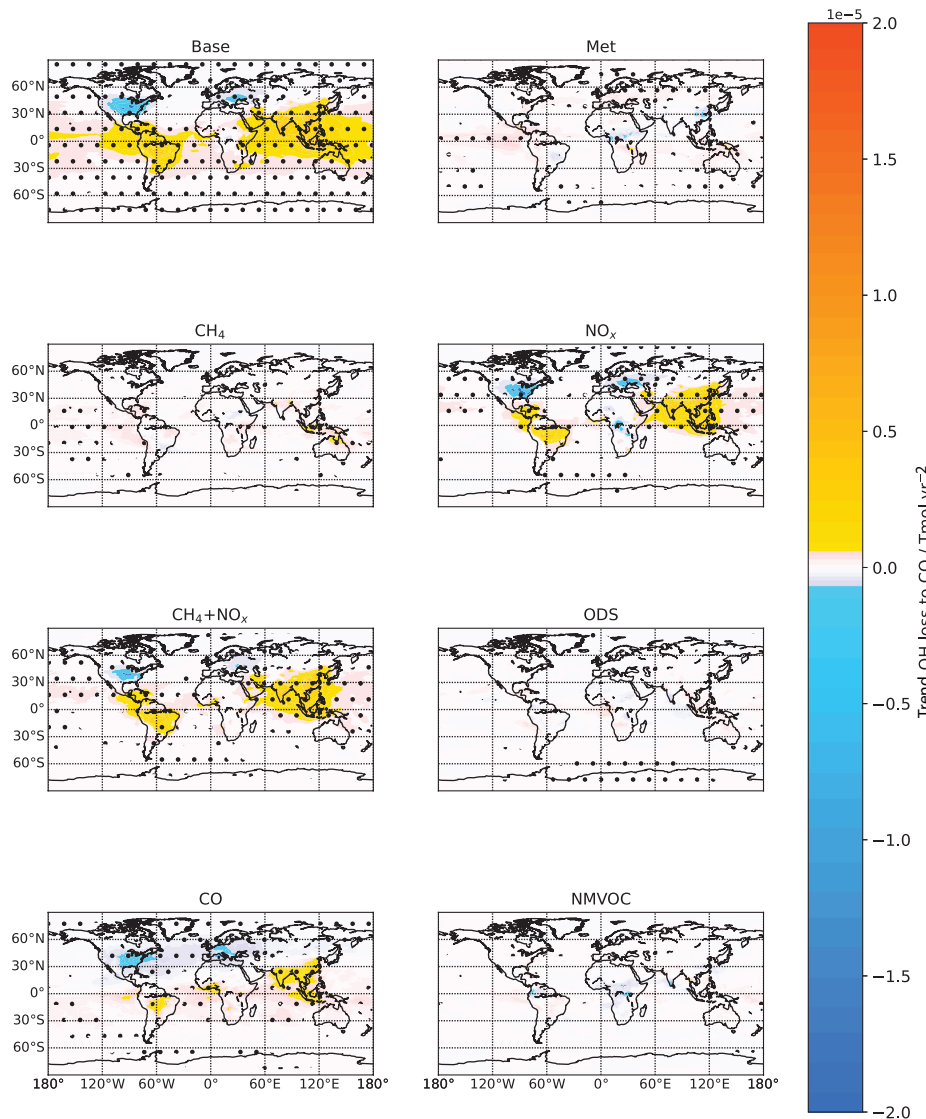
Figure 8. Tropospheric airmass-weighted OH loss flux to reaction with CO spatial trends from 1980 to 2014 for the different model runs. Trends and stippling are as per Fig. 3. Regions of decreasing CO emissions see decreasing OH loss via reaction with CO and hence an increase in [OH] (as seen in the 'CO' run in Fig. 3), and vice versa.

and environmental policies, the reason for biases in the global bottom-up inventories is that they may lack the latest data about regional activity and emission factor changes, and so in these cases using regional or top-down inventories might reduce biases.

There are various implications of the model-observations mismatch. Given what we understand about how CO affects modelled [OH] in the GFDL AM4.1 from our earlier analyses, we could suspect that, in places where we underestimate the
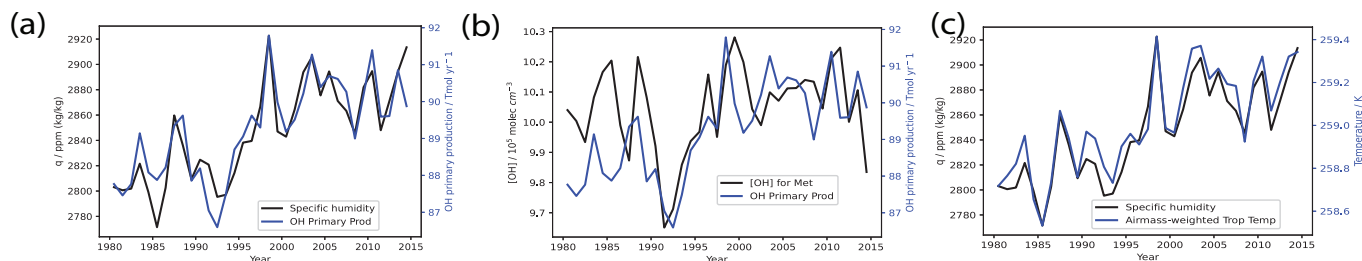
Figure 9. OH primary production and [OH] in the meteorology-driven ('Met') run. (a) shows the comparison between specific humidity (lefthand axis, black) and OH primary production (righthand axis, blue) in the meteorology-driven run; (b) shows the [OH] (lefthand axis, black) compared with OH primary production (righthand axis, blue); and (c) shows the comparison between specific humidity (lefthand axis, black) and tropospheric airmass-weighted air temperature (righthand axis, blue). Meteorology plays an important role for IAV in OH primary production, with OH primary production being strongly correlated with changes in specific humidity (q) (r = 0.90) which itself is strongly correlated with temperature (r = 0.96).
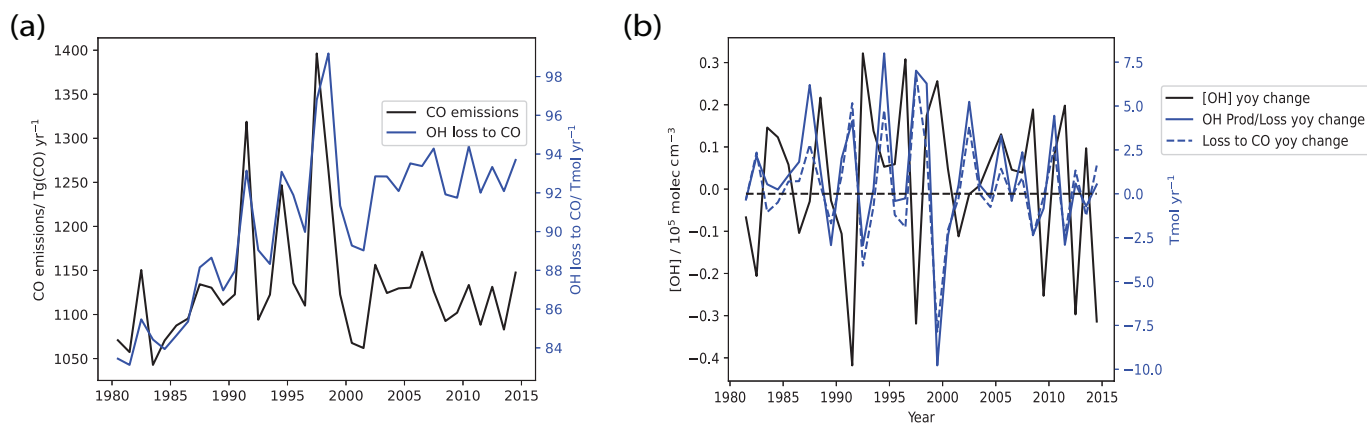
Figure 10. Plots of (a) OH loss to CO with CO emissions, and (b) the year-on-year changes in [OH] together with the year-on-year changes in net OH production and that of OH loss to CO. As seen in (a), CO emissions are positively correlated with OH loss to CO in the 'Base' run ($r = 0.69$). This thereafter drives overall IAV in total loss and production. As seen in (b), we see that OH year-on-year production/loss change (solid blue) is highly correlated with that of the OH loss to CO (dotted blue) with $r = 0.94$, suggesting that the OH loss to CO is indeed driving the IAV seen in total production/loss. The year-on-year change in production/loss, in turn, is anti-correlated with the year-on-year change in OH, with $r = -0.36$.

405   decreasing trend, we could be underestimating the [OH] increase due to decreasing CO. Meanwhile, in those areas where we model a CO increase when observations suggest a decrease instead, we may be modelling an [OH] decrease due to increasing CO in those regions, as opposed to an [OH] increase due to decreasing CO. Overall, this means that, globally, we could be underestimating the [OH] increase over the 2001-2014 period.

We next evaluate the IAV captured in the model against that observed from MOPITT, by comparing the area-weighted global (60°S-60°N) mean 12-month rolling mean CO columns with MOPITT observations over the 2001-2014 period in Fig. 11(c) and the detrended series in Fig. 11(d). From Fig. 11(c), we see again that the model underestimates the decreasing trend seen in MOPITT, with the model trend of -0.021×10^{18}molec cm^{-2} yr^{-1} being five times as small in magnitude as the MOPITT trend of -0.10×10^{18}molec cm^{-2} yr^{-1}, which reinforces the analysis from Fig. 11(a) and (b). However, we see that the model captures the IAV well, with the Pearson coefficient $r = 0.62$ and $r = 0.76$ for the raw and detrended time series respectively. Given that the main driver of our modelled CO IAV comes from the biomass burning emission inventory used, this could rule out the biomass burning emission inventory used as a cause of the model-observations mismatch. Furthermore, given the prominent role that CO plays in driving the modelled [OH] IAV, our findings here also suggest that our model is capturing the [OH] IAV due to CO well from 2005-2014.

4.2 NO$_x$: Comparison of Tropospheric NO$_2$ Column with OMI

Fig. 12(a) shows the annual mean OMI tropospheric NO$_2$ column and modelled NO$_2$ column trends from 2005 to 2014, and Fig. 12(b) shows the input NO$_x$ emission trends over the same time period. We see that there is general agreement between the emissions and the model tropospheric NO$_2$ column. Also, both show significant positive trends over South Asia and Eastern China, and significant negative trends over Eastern USA and Western Europe. These, in turn, are also consistent with the OMI tropospheric NO$_2$ column observations (the OMI observations over the remote ocean are likely to have large errors due to the observational detection limit.) From the literature, Miyazaki et al. (2017), who looked at an assimilation of multiple satellite datasets, including the OMI NO$_2$ column, obtained a global non-lightning NO$_x$ emission from 2005 to 2014 of a roughly constant value of 47.9TgN/yr. This also agrees well with the emissions inventory used in our model, as shown in Fig. 1(c), where, even though we are slightly high-biased (about 8% higher), our global NO$_x$ emissions are also stable from 2005 to 2014. Overall, these findings lend confidence in our model NO$_x$ trends from 2005 to 2014.

5 Conclusions

In this study, we systematically analyzed the sensitivity of [OH] to changes in drivers of OH over the 1980-2014 period using the GFDL AM4.1 model. We attribute the [OH] changes to changes in emissions and meteorology individually as opposed to a lumped approach adopted in the multimodel study by Stevenson et al. (2020). Such a decomposition allows for a clearer mechanistic understanding of the main driving factors of either the trend or IAV. In addition, we analysed the OH budget terms, similar to Zhao et al. (2020), tracing the individual emissions to changes in the various budget terms, which in turn affects [OH].

We found that annual mean global tropospheric airmass-weighted [OH] has increased by $\sim 10\%$ compared to the 1998-2007 mean from 1980 to 2014, in agreement with multimodel comparisons of ESMs by Stevenson et al. (2020), and furthermore has increased by $\sim 5\%$ in 2014 compared to 1980, in agreement with multi-model studies such as from ACCMIP (Naik et al., 2013) and CCMI (Zhao et al., 2019). This modelled increasing [OH] trend, especially post-2007, is in contrast with the absence
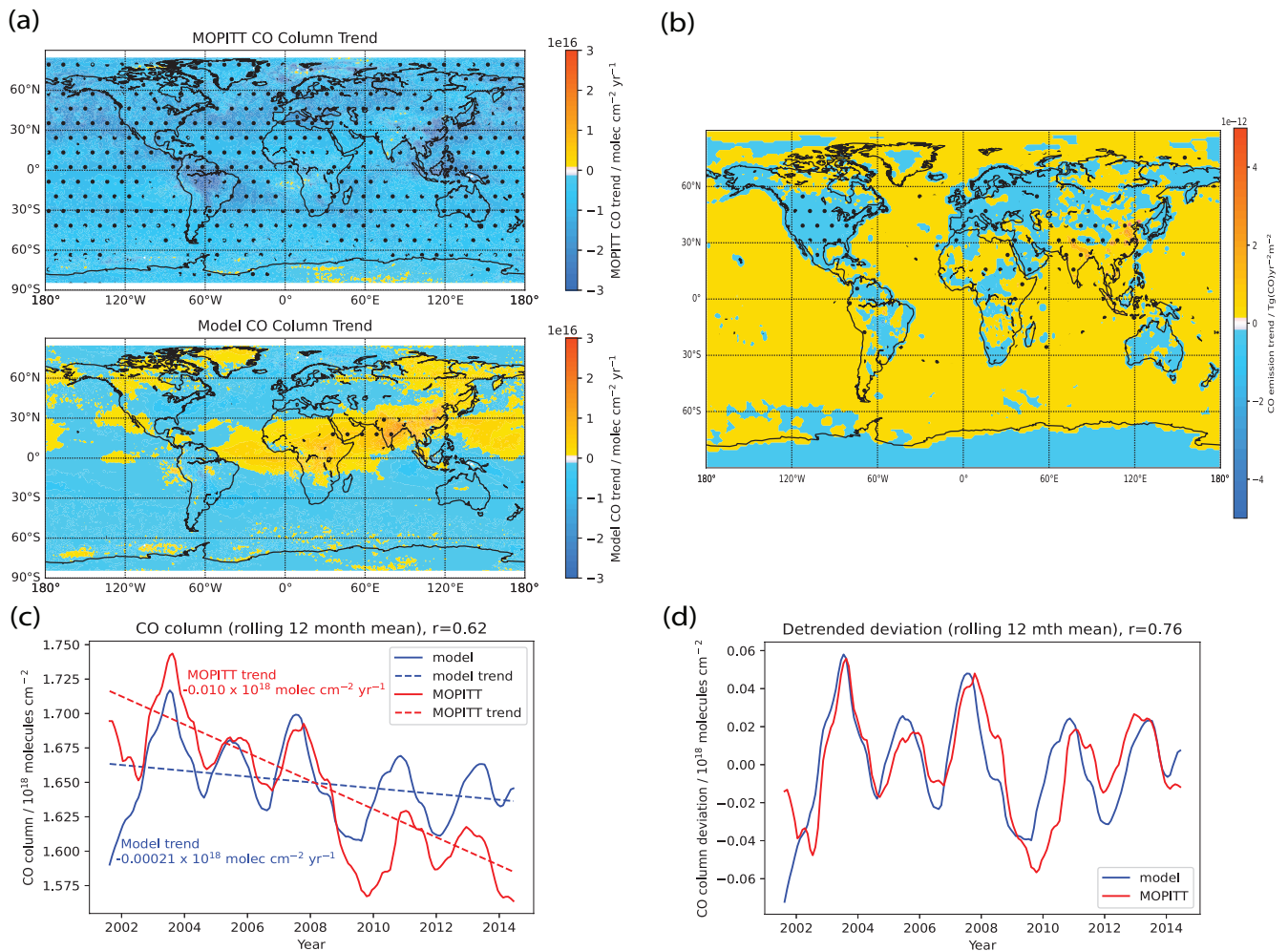
Figure 11. (a) Model comparison of annual mean CO column trends with MOPITT observations over the 2001-2014 period, (b) CO emission trends over the 2001-2014 period, (c) model comparison of area-weighted global (60°S-60°N) mean 12-month rolling mean CO columns with MOPITT observations over the 2001-2014 period, and (d) model comparison of area-weighted global (60°S-60°N) 12-month rolling mean detrended CO columns with MOPITT observations over the 2001-2014 period. Trends and stippling in (a) and (b) are as per Fig. 3. For (c), the dotted lines represent the linear trendline as calculated using the Theil-Sen method. The MOPITT CO column generally sees significant negative trends throughout the spatial domain. However, the modelled CO columns show mixed trends which mirror the CO emission trends as seen in (b), especially the increasing trend over China and South Asia, and are in poor agreement with trends derived from MOPITT. We can also see from (c) that the model underestimates the negative trend seen in MOPITT. However, from (c) and (d), we see that the model captures the MOPITT IAV well, with Pearson correlation coefficient of $r = 0.62$ and $r = 0.76$ for the raw and detrended time series respectively.
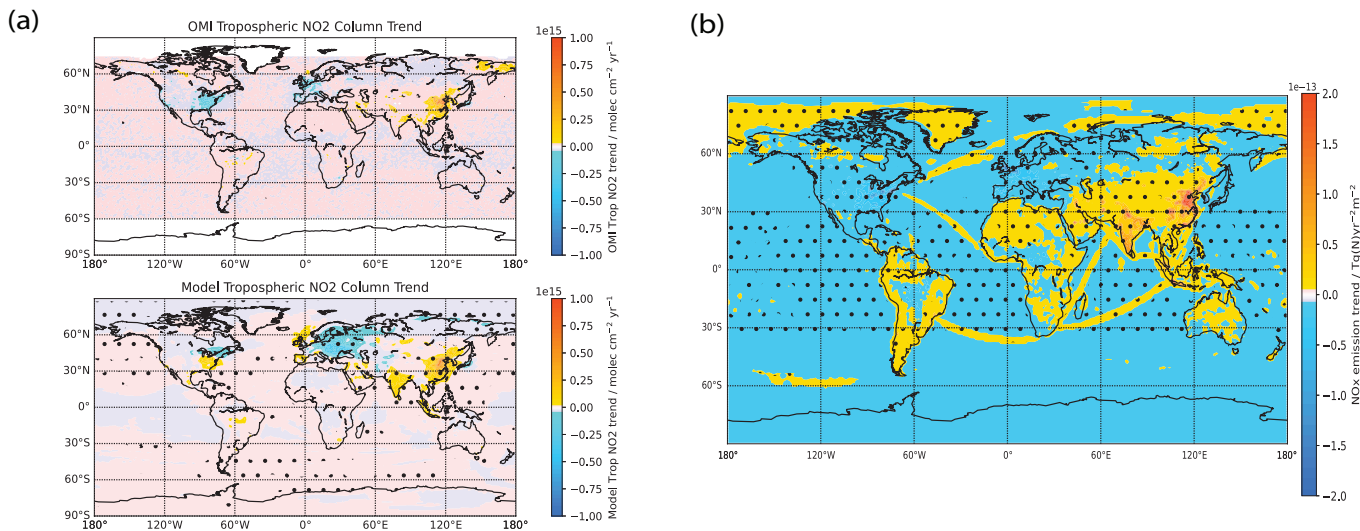
Figure 12. (a) Model comparison of annual mean tropospheric NO_2 column trends with OMI tropospheric NO_2 observations processed by Goldberg et al. (2021) over the 2005-2014 period, and (b) NO_x emission trends over the 2005-2014 period. Trends and stippling are as per Fig. 3. We see that there is general agreement between the emissions and the model tropospheric NO_2 column. Also, both show significant positive trends over South Asia and Eastern China, and significant negative trends over Eastern USA and Western Europe. These, in turn, are also consistent with the OMI tropospheric NO_2 column observations. Overall, these findings lend confidence in our model NO_x trends from 2005 to 2014.

of change (e.g., Nicely et al., 2020; Patra et al., 2021) or decreasing [OH] (e.g., Rigby et al., 2017; Turner et al., 2017) derived from observationally-constrained inversion methods.

In our model, the increasing trend in [OH] is caused by the net effects of increasing NO_x emissions, which increases [OH] via both primary and secondary [OH] production, balanced by the increase in CH_4 concentrations which tend to consume OH. The combined effects of NO_x emissions and CH_4 concentrations can account for the spatial distribution of the [OH] trends as well. These findings agree with other studies, such as Naik et al. (2013), who also suggested the importance of NO_x and CH_4 in driving the modelled [OH] trend. Locally, CO emissions, meteorology and NMVOC emissions also play an important role in driving the increasing [OH] trend, but their effects average out on the global level. Meanwhile, the observed [OH] IAV is dominated by impacts from the IAV in biomass burning CO emissions as well as meteorology.

We also found, while our model does a good job in matching MOPITT CO column IAV over the 2001-2014 period, our model does a poor job of matching MOPITT total column CO trends over the 2001-2014 period. Given that modelled column CO trends were driven by input CO emission trends, this could in turn point towards some deficiencies in the input emissions. Zheng et al. (2019) further suggest that emissions from CEDS, which is the anthropogenic CO emissions dataset used in our study, are inconsistent for China and South Asia. Whereas CEDS suggests rapidly increasing CO from China and South Asia, Zheng et al. (2019) found instead a decreasing trend for China and a modestly-increasing one for South Asia. The increasing

CO trends from China and South Asia, in turn, lead to higher CO levels. Additionally, we found that the modelled tropospheric NO_2 column trends qualitatively agree with OMI satellite tropospheric NO_2 column trends over the 2005-2014 period. Thus, overall, the underestimated declining trend in CO emissions in our model could mean that the actual modelled [OH] increase is larger than what was currently modelled.

5.1 Discussion

Overall, based on the current set-up, the AM4.1 models an increase in tropospheric [OH] from 1980 to 2014. This is even in the backdrop of the increase in CH_4 throughout the period. As seen in Fig. 13, this causes the CH_4 lifetime with respect to OH (calculated via the global annual mean atmospheric CH_4 burden divided by annual mean CH_4 tropospheric chemical loss by OH) to decrease in the 'Base' run by about 10%. In the absence of other changes, one would expect the increase in CH_4 to reduce [OH], thereby further prolonging the CH_4 lifetime, which we in fact do see in Fig. 13 in the 'CH_4' run. Instead, we see that the increase in NO_x together with the stalling of CO has led to a greater increase in [OH] than would be expected by the increase in CH_4, such that CH_4 lifetime still continues to decrease. This helps to slow the accumulation of CH_4 in the atmosphere. If what we found in this study is true and [OH] has indeed increased, this could suggest that studies trying to derive CH_4 emissions from observed CH_4 concentrations will underestimate CH_4 emissions if they do not take into account the increasing [OH]. We acknowledge that CH_4 concentrations are prescribed on the surface in the current model set-up, so this can lead to an underestimation of the surface chemical feedbacks. Including the surface feedbacks would likely amplify the modelled effects of CH_4 on [OH]. This will be further investigated in an emissions-driven run.

Also, in the future, should aggressive air quality policies cause a reduction in NO_x emissions, this could cause the [OH] to decrease, thereby further accelerating the buildup of CH_4 in the atmosphere. On the other hand, if CO emissions also decrease concomitantly, this could offset the NO_x reduction effects on [OH]. Future work could involve looking at how [OH] evolves under future scenarios, such as the Shared Socioeconomic Pathways (SSPs) formulated as part of CMIP6. In particular, future work could focus on whether NO_x and CO will still play a dominant role in the future, under different scenarios of climate change as well as emissions reductions. The recent COVID-19 related large reduction in emissions in cities across the world have provided a glimpse of what could happen in future scenarios. For example, Laughner et al. (2021) found that the decrease in NO_x emissions in 2020 led to a decrease in ozone which thereby led to a 2-4% decrease in global [OH], and this could have contributed to the large $[CH_4]$ growth rate that year. This was further corroborated by Stevenson et al. (2022) and Peng et al. (2022) who both found that about half of the large $[CH_4]$ growth rate was attributed to the decline in [OH] due to declining NO_x. Peng et al. (2022) also additionally showed that the effect of declining NO_x emissions which led to decreased [OH] overwhelmed the impacts of the decline of other NTCFs like CO emissions. NO_x emissions have since largely returned back to pre-pandemic levels, and this could drive [OH] increases again. In the backdrop of the anthropogenic emission changes, the pandemic years have also seen many large wildfire events as well, and the associated biomass burning emissions could also impact [OH]. Overall, these could be interesting test cases to explore in ESMs with interactive chemistry.

In our paper, we explored the role of meteorology and input emission inventories in driving the [OH] trend during the 1980-2014 period, but, as Murray et al. (2021) points out, there are many other factors within models that could be important
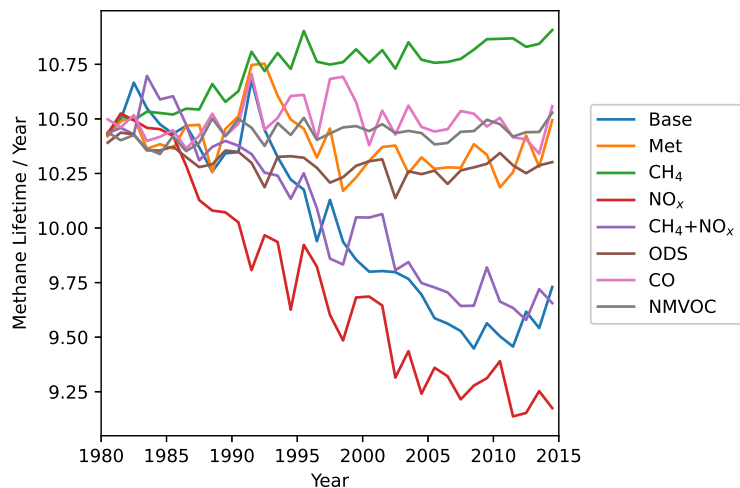
Figure 13. CH_4 lifetime with respect to oxidation by OH for the different model runs. CH_4 lifetime is calculated via the global annual mean atmospheric CH_4 burden divided by annual mean CH_4 tropospheric chemical loss by OH. CH_4 lifetime has decreased in the 'Base' run even as CH_4 concentrations have increased, driven by [OH] increases.

490   in driving inter- and intra-model [OH] variations, with key factors being the details of the implemented chemical scheme, which has implications on oxidation of VOCs into CO and NO_x lifetime, as well as other physical parameterizations, such as lightning NO_x altitude which also affects NO_x lifetime. The importance of understanding the CO budget drivers and potential biases is further underscored by the existing biases present in the GFDL AM4.1, such as in the seasonal mean CO column (Horowitz et al., 2020) and the CO column trend. Nonetheless, given that we have identified various input emission drivers as

495   playing a key role in driving the increasing [OH] trend over the 1980-2014 period, and other models participating in CMIP6 also have likely used the same anthropogenic emission inventories, our study could also serve as a motivation to do a similar sensitivity analysis in other CCMs, such as the other ESMs studied in Stevenson et al. (2020). This could help elucidate the role of emissions in driving the multi-model mean trend, and potentially further emphasize the importance of accurate short-lived climate forcer emission inventories for both climate and air quality projections (Smith et al., 2022).

500   *Code and data availability.* The code and data used in this paper are available upon request.

Author contributions. GC wrote the text and performed the main analysis. VN and LWH helped to conceptualize the study and provided comments.

Competing interests. The contact author has declared that none of the authors has any competing interests.

Acknowledgements. This work was prepared by GC under award NA18OAR4320123 from the National Oceanic and Atmospheric Administration, U.S. Department of Commerce. The statements, findings, conclusions, and recommendations are those of the author(s) and do not necessarily reflect the views of the National Oceanic and Atmospheric Administration, or the U.S. Department of Commerce. We acknowledge GFDL HPC resources without which the AM4.1 simulations would not have been possible. We also acknowledge Jian He who provided additional comments as well as help with the MOPITT, and Daniel Goldberg for the processed gridded version 4 OMI data used in this study. We also acknowledge the two internal reviewers Chloe Gao and Meiyun Lin for their useful comments.

References

Alexander, B. and Mickley, L. J.: Paleo-Perspectives on Potential Future Changes in the Oxidative Capacity of the Atmosphere Due to Climate Change and Anthropogenic Emissions, Current Pollution Reports, 1, 57–69, https://doi.org/10.1007/s40726-015-0006-0, 2015.

Anderson, D. C., Duncan, B. N., Fiore, A. M., Baublitz, C. B., Follette-Cook, M. B., Nicely, J. M., and Wolfe, G. M.: Spatial and temporal variability in the hydroxyl (OH) radical: understanding the role of large-scale climate features and their influence on OH through its dynamical and photochemical drivers, Atmospheric Chemistry and Physics, 21, 6481–6508, https://doi.org/10.5194/acp-21-6481-2021, 2021.

Bian, H. and Prather, M. J.: Fast-J2: Accurate Simulation of Stratospheric Photolysis in Global Chemical Models, Journal of Atmospheric Chemistry, 41, 281–296, https://doi.org/10.1023/a:1014980619462, 2002.

Brasseur, G. P. and Solomon, S.: Aeronomy of the Middle Atmosphere, Springer Netherlands, https://doi.org/10.1007/1-4020-3824-0, 2005.

Crutzen, P. J. and Lawrence, M. G.: The impact of precipitation scavenging on the transport of trace gases: A 3-dimensional model sensitivity study, Journal of Atmospheric Chemistry, 37, 81–112, https://doi.org/10.1023/a:1006322926426, 2000.

Deeter, M. N.: Operational carbon monoxide retrieval algorithm and selected results for the MOPITT instrument, Journal of Geophysical Research, 108, https://doi.org/10.1029/2002jd003186, 2003.

Deeter, M. N., Edwards, D. P., Francis, G. L., Gille, J. C., Mao, D., Martínez-Alonso, S., Worden, H. M., Ziskin, D., and Andreae, M. O.: Radiance-based retrieval bias mitigation for the MOPITT instrument: the version 8 product, Atmospheric Measurement Techniques, 12, 4561–4580, https://doi.org/10.5194/amt-12-4561-2019, 2019.

Elguindi, N., Granier, C., Stavrakou, T., Darras, S., Bauwens, M., Cao, H., Chen, C., van der Gon, H. A. C. D., Dubovik, O., Fu, T. M., Henze, D. K., Jiang, Z., Keita, S., Kuenen, J. J. P., Kurokawa, J., Liousse, C., Miyazaki, K., Müller, J.-F., Qu, Z., Solmon, F., and Zheng, B.: Intercomparison of Magnitudes and Trends in Anthropogenic Surface Emissions From Bottom-Up Inventories, Top-Down Estimates, and Emission Scenarios, Earth's Future, 8, https://doi.org/10.1029/2020ef001520, 2020.

Eskes, H. J. and Boersma, K. F.: Averaging kernels for DOAS total-column satellite retrievals, Atmospheric Chemistry and Physics, 3, 1285–1291, https://doi.org/10.5194/acp-3-1285-2003, 2003.

Fiore, A. M., Horowitz, L. W., Dlugokencky, E. J., and West, J. J.: Impact of meteorology and emissions on methane trends, 1990–2004, Geophysical Research Letters, 33, https://doi.org/10.1029/2006gl026199, 2006.

Goldberg, D. L., Anenberg, S. C., Lu, Z., Streets, D. G., Lamsal, L. N., McDuffie, E. E., and Smith, S. J.: Urban NOx emissions around the world declined faster than anticipated between 2005 and 2019, Environmental Research Letters, 16, 115 004, https://doi.org/10.1088/1748-9326/ac2c34, 2021.

Granier, C., Lamarque, J., Mieville, A., Muller, J., Olivier, J., Orlando, J., Peters, J., Petron, G., Tyndall, G., and Wallens, S.: POET, a database of surface emissions of ozone precursors, 2005.

Hameed, S., Pinto, J. P., and Stewart, R. W.: Sensitivity of the predicted CO-OH-CH4 perturbation to tropospheric NOx concentrations, Journal of Geophysical Research, 84, 763, https://doi.org/10.1029/jc084ic02p00763, 1979.

He, J., Naik, V., Horowitz, L. W., Dlugokencky, E., and Thoning, K.: Investigation of the global methane budget over 1980–2017 using GFDL-AM4.1, Atmospheric Chemistry and Physics, 20, 805–827, https://doi.org/10.5194/acp-20-805-2020, 2020.

He, J., Naik, V., and Horowitz, L. W.: Hydroxyl Radical (OH) Response to Meteorological Forcing and Implication for the Methane Budget, Geophysical Research Letters, 48, https://doi.org/10.1029/2021gl094140, 2021.

Hoesly, R. M., Smith, S. J., Feng, L., Klimont, Z., Janssens-Maenhout, G., Pitkanen, T., Seibert, J. J., Vu, L., Andres, R. J., Bolt, R. M., Bond, T. C., Dawidowski, L., Kholod, N., ichi Kurokawa, J., Li, M., Liu, L., Lu, Z., Moura, M. C. P., O'Rourke, P. R., and Zhang, Q.: Historical (1750–2014) anthropogenic emissions of reactive gases and aerosols from the Community Emissions Data System (CEDS), Geoscientific Model Development, 11, 369–408, https://doi.org/10.5194/gmd-11-369-2018, 2018.

550 Holmes, C. D., Prather, M. J., Søvde, O. A., and Myhre, G.: Future methane, hydroxyl, and their uncertainties: key climate and emission parameters for future predictions, Atmospheric Chemistry and Physics, 13, 285–302, https://doi.org/10.5194/acp-13-285-2013, 2013.

Horowitz, L. W., Naik, V., Paulot, F., Ginoux, P. A., Dunne, J. P., Mao, J., Schnell, J., Chen, X., He, J., John, J. G., Lin, M., Lin, P., Malyshev, S., Paynter, D., Shevliakova, E., and Zhao, M.: The GFDL Global Atmospheric Chemistry-Climate Model AM4.1: Model Description and Simulation Characteristics, Journal of Advances in Modeling Earth Systems, 12, https://doi.org/10.1029/2019ms002032, 2020.

555 Jacob, D. J.: Introduction to Atmospheric Chemistry, Princeton University Press, https://doi.org/10.1515/9781400841547, 2000.

Jaeglé, L., Jacob, D. J., Brune, W. H., and Wennberg, P. O.: Chemistry of HOx radicals in the upper troposphere, Atmospheric Environment, 35, 469–489, https://doi.org/10.1016/s1352-2310(00)00376-9, 2001.

Lamsal, L. N., Krotkov, N. A., Vasilkov, A., Marchenko, S., Qin, W., Yang, E.-S., Fasnacht, Z., Joiner, J., Choi, S., Haffner, D., Swartz, W. H., Fisher, B., and Bucsela, E.: Ozone Monitoring Instrument (OMI) Aura nitrogen dioxide standard product version 4.0 with improved surface 560 and cloud treatments, Atmospheric Measurement Techniques, 14, 455–479, https://doi.org/10.5194/amt-14-455-2021, 2021.

Laughner, J. L., Neu, J. L., Schimel, D., Wennberg, P. O., Barsanti, K., Bowman, K. W., Chatterjee, A., Croes, B. E., Fitzmaurice, H. L., Henze, D. K., Kim, J., Kort, E. A., Liu, Z., Miyazaki, K., Turner, A. J., Anenberg, S., Avise, J., Cao, H., Crisp, D., de Gouw, J., Eldering, A., Fyfe, J. C., Goldberg, D. L., Gurney, K. R., Hasheminassab, S., Hopkins, F., Ivey, C. E., Jones, D. B. A., Liu, J., Lovenduski, N. S., Martin, R. V., McKinley, G. A., Ott, L., Poulter, B., Ru, M., Sander, S. P., Swart, N., Yung, Y. L., and and, Z.-C. Z.: Societal shifts due to 565 COVID-19 reveal large-scale complexities and feedbacks between atmospheric chemistry and climate change, Proceedings of the National Academy of Sciences, 118, https://doi.org/10.1073/pnas.2109481118, 2021.

Lawrence, M. G., Jöckel, P., and von Kuhlmann, R.: What does the global mean OH concentration tell us?, Atmospheric Chemistry and Physics, 1, 37–49, https://doi.org/10.5194/acp-1-37-2001, 2001.

Lawrence, M. G., von Kuhlmann, R., Salzmann, M., and Rasch, P. J.: The balance of effects of deep convective mixing on tropospheric 570 ozone, Geophysical Research Letters, 30, https://doi.org/10.1029/2003gl017644, 2003.

Lelieveld, J., Gromov, S., Pozzer, A., and Taraborrelli, D.: Global tropospheric hydroxyl distribution, budget and reactivity, Atmospheric Chemistry and Physics, 16, 12 477–12 493, https://doi.org/10.5194/acp-16-12477-2016, 2016.

Levy, H.: Normal Atmosphere: Large Radical and Formaldehyde Concentrations Predicted, Science, 173, 141–143, https://doi.org/10.1126/science.173.3992.141, 1971.

575 Mao, J., Fan, S., Jacob, D. J., and Travis, K. R.: Radical loss in the atmosphere from Cu-Fe redox coupling in aerosols, Atmospheric Chemistry and Physics, 13, 509–519, https://doi.org/10.5194/acp-13-509-2013, 2013a.

Mao, J., Horowitz, L. W., Naik, V., Fan, S., Liu, J., and Fiore, A. M.: Sensitivity of tropospheric oxidants to biomass burning emissions: implications for radiative forcing, Geophysical Research Letters, 40, 1241–1246, https://doi.org/10.1002/grl.50210, 2013b.

Meinshausen, M., Vogel, E., Nauels, A., Lorbacher, K., Meinshausen, N., Etheridge, D. M., Fraser, P. J., Montzka, S. A., Rayner, P. J., 580 Trudinger, C. M., Krummel, P. B., Beyerle, U., Canadell, J. G., Daniel, J. S., Enting, I. G., Law, R. M., Lunder, C. R., O'Doherty, S., Prinn, R. G., Reimann, S., Rubino, M., Velders, G. J. M., Vollmer, M. K., Wang, R. H. J., and Weiss, R.: Historical greenhouse gas concentrations for climate modelling (CMIP6), Geoscientific Model Development, 10, 2057–2116, https://doi.org/10.5194/gmd-10-2057-2017, 2017.

Miyazaki, K., Eskes, H., Sudo, K., Boersma, K. F., Bowman, K., and Kanaya, Y.: Decadal changes in global surface NO_x emissions from multi-constituent satellite data assimilation, Atmospheric Chemistry and Physics, 17, 807–837, https://doi.org/10.5194/acp-17-807-2017, 2017.

Montzka, S. A., Krol, M., Dlugokencky, E., Hall, B., Jockel, P., and Lelieveld, J.: Small Interannual Variability of Global Atmospheric Hydroxyl, Science, 331, 67–69, https://doi.org/10.1126/science.1197640, 2011.

Murray, L. T., Logan, J. A., and Jacob, D. J.: Interannual variability in tropical tropospheric ozone and OH: The role of lightning, Journal of Geophysical Research: Atmospheres, 118, 11,468–11,480, https://doi.org/10.1002/jgrd.50857, 2013.

Murray, L. T., Mickley, L. J., Kaplan, J. O., Sofen, E. D., Pfeiffer, M., and Alexander, B.: Factors controlling variability in the oxidative capacity of the troposphere since the Last Glacial Maximum, Atmospheric Chemistry and Physics, 14, 3589–3622, https://doi.org/10.5194/acp-14-3589-2014, 2014.

Murray, L. T., Fiore, A. M., Shindell, D. T., Naik, V., and Horowitz, L. W.: Large uncertainties in global hydroxyl projections tied to fate of reactive nitrogen and carbon, Proceedings of the National Academy of Sciences, 118, https://doi.org/10.1073/pnas.2115204118, 2021.

Naik, V., Voulgarakis, A., Fiore, A. M., Horowitz, L. W., Lamarque, J.-F., Lin, M., Prather, M. J., Young, P. J., Bergmann, D., Cameron-Smith, P. J., Cionni, I., Collins, W. J., Dalsøren, S. B., Doherty, R., Eyring, V., Faluvegi, G., Folberth, G. A., Josse, B., Lee, Y. H., MacKenzie, I. A., Nagashima, T., van Noije, T. P. C., Plummer, D. A., Righi, M., Rumbold, S. T., Skeie, R., Shindell, D. T., Stevenson, D. S., Strode, S., Sudo, K., Szopa, S., and Zeng, G.: Preindustrial to present-day changes in tropospheric hydroxyl radical and methane lifetime from the Atmospheric Chemistry and Climate Model Intercomparison Project (ACCMIP), Atmospheric Chemistry and Physics, 13, 5277–5298, https://doi.org/10.5194/acp-13-5277-2013, 2013.

Naus, S., Montzka, S. A., Pandey, S., Basu, S., Dlugokencky, E. J., and Krol, M.: Constraints and biases in a tropospheric two-box model of OH, Atmospheric Chemistry and Physics, 19, 407–424, https://doi.org/10.5194/acp-19-407-2019, 2019.

Naus, S., Montzka, S. A., Patra, P. K., and Krol, M. C.: A three-dimensional-model inversion of methyl chloroform to constrain the atmospheric oxidative capacity, Atmospheric Chemistry and Physics, 21, 4809–4824, https://doi.org/10.5194/acp-21-4809-2021, 2021.

Nicely, J. M., Canty, T. P., Manyin, M., Oman, L. D., Salawitch, R. J., Steenrod, S. D., Strahan, S. E., and Strode, S. A.: Changes in Global Tropospheric OH Expected as a Result of Climate Change Over the Last Several Decades, Journal of Geophysical Research: Atmospheres, 123, https://doi.org/10.1029/2018jd028388, 2018.

Nicely, J. M., Duncan, B. N., Hanisco, T. F., Wolfe, G. M., Salawitch, R. J., Deushi, M., Haslerud, A. S., Jöckel, P., Josse, B., Kinnison, D. E., Klekociuk, A., Manyin, M. E., Marécal, V., Morgenstern, O., Murray, L. T., Myhre, G., Oman, L. D., Pitari, G., Pozzer, A., Quaglia, I., Revell, L. E., Rozanov, E., Stenke, A., Stone, K., Strahan, S., Tilmes, S., Tost, H., Westervelt, D. M., and Zeng, G.: A machine learning examination of hydroxyl radical differences among model simulations for CCMI-1, Atmospheric Chemistry and Physics, 20, 1341–1361, https://doi.org/10.5194/acp-20-1341-2020, 2020.

Nisbet, E. G., Dlugokencky, E. J., Fisher, R. E., France, J. L., Lowry, D., Manning, M. R., Michel, S. E., and Warwick, N. J.: Atmospheric methane and nitrous oxide: challenges alongthe path to Net Zero, Philosophical Transactions of the Royal Society A: Mathematical, Physical and Engineering Sciences, 379, 20200 457, https://doi.org/10.1098/rsta.2020.0457, 2021.

Patra, P. K., Krol, M. C., Prinn, R. G., Takigawa, M., Mühle, J., Montzka, S. A., Lal, S., Yamashita, Y., Naus, S., Chandra, N., Weiss, R. F., Krummel, P. B., Fraser, P. J., O'Doherty, S., and Elkins, J. W.: Methyl Chloroform Continues to Constrain the Hydroxyl (OH) Variability in the Troposphere, Journal of Geophysical Research: Atmospheres, 126, https://doi.org/10.1029/2020jd033862, 2021.

Peng, S., Lin, X., Thompson, R. L., Xi, Y., Liu, G., Hauglustaine, D., Lan, X., Poulter, B., Ramonet, M., Saunois, M., Yin, Y., Zhang, Z., Zheng, B., and Ciais, P.: Wetland emission and atmospheric sink changes explain methane growth in 2020, Nature, 612, 477–482, https://doi.org/10.1038/s41586-022-05447-w, 2022.

Pickering, K. E., Wang, Y., Tao, W.-K., Price, C., and Müller, J.-F.: Vertical distributions of lightning NOx for use in regional and global chemical transport models, Journal of Geophysical Research: Atmospheres, 103, 31 203–31 216, https://doi.org/10.1029/98jd02651, 1998.

Price, C., Penner, J., and Prather, M.: NOx from lightning: 1. Global distribution based on lightning physics, Journal of Geophysical Research: Atmospheres, 102, 5929–5941, https://doi.org/10.1029/96jd03504, 1997.

Rasmussen, D., Fiore, A., Naik, V., Horowitz, L., McGinnis, S., and Schultz, M.: Surface ozone-temperature relationships in the eastern US: A monthly climatology for evaluating chemistry-climate models, Atmospheric Environment, 47, 142–153, https://doi.org/10.1016/j.atmosenv.2011.11.021, 2012.

Rigby, M., Montzka, S. A., Prinn, R. G., White, J. W. C., Young, D., O'Doherty, S., Lunt, M. F., Ganesan, A. L., Manning, A. J., Simmonds, P. G., Salameh, P. K., Harth, C. M., Mühle, J., Weiss, R. F., Fraser, P. J., Steele, L. P., Krummel, P. B., McCulloch, A., and Park, S.: Role of atmospheric oxidation in recent methane growth, Proceedings of the National Academy of Sciences, 114, 5373–5377, https://doi.org/10.1073/pnas.1616426114, 2017.

Saunois, M., Stavert, A. R., Poulter, B., Bousquet, P., Canadell, J. G., Jackson, R. B., Raymond, P. A., Dlugokencky, E. J., Houweling, S., Patra, P. K., Ciais, P., Arora, V. K., Bastviken, D., Bergamaschi, P., Blake, D. R., Brailsford, G., Bruhwiler, L., Carlson, K. M., Carrol, M., Castaldi, S., Chandra, N., Crevoisier, C., Crill, P. M., Covey, K., Curry, C. L., Etiope, G., Frankenberg, C., Gedney, N., Hegglin, M. I., Höglund-Isaksson, L., Hugelius, G., Ishizawa, M., Ito, A., Janssens-Maenhout, G., Jensen, K. M., Joos, F., Kleinen, T., Krummel, P. B., Langenfelds, R. L., Laruelle, G. G., Liu, L., Machida, T., Maksyutov, S., McDonald, K. C., McNorton, J., Miller, P. A., Melton, J. R., Morino, I., Müller, J., Murguia-Flores, F., Naik, V., Niwa, Y., Noce, S., O'Doherty, S., Parker, R. J., Peng, C., Peng, S., Peters, G. P., Prigent, C., Prinn, R., Ramonet, M., Regnier, P., Riley, W. J., Rosentreter, J. A., Segers, A., Simpson, I. J., Shi, H., Smith, S. J., Steele, L. P., Thornton, B. F., Tian, H., Tohjima, Y., Tubiello, F. N., Tsuruta, A., Viovy, N., Voulgarakis, A., Weber, T. S., van Weele, M., van der Werf, G. R., Weiss, R. F., Worthy, D., Wunch, D., Yin, Y., Yoshida, Y., Zhang, W., Zhang, Z., Zhao, Y., Zheng, B., Zhu, Q., Zhu, Q., and Zhuang, Q.: The Global Methane Budget 2000–2017, Earth System Science Data, 12, 1561–1623, https://doi.org/10.5194/essd-12-1561-2020, 2020.

Smith, S., McDuffie, E. E., and Charles, M.: Opinion: Coordinated Development of Emission Inventories for Climate Forcers and Air Pollutants, Atmospheric Chemistry and Physics, 22, 13 201–13 218, https://doi.org/10.5194/acp-22-13201-2022, in review, 2022.

Spivakovsky, C. M., Logan, J. A., Montzka, S. A., Balkanski, Y. J., Foreman-Fowler, M., Jones, D. B. A., Horowitz, L. W., Fusco, A. C., Brenninkmeijer, C. A. M., Prather, M. J., Wofsy, S. C., and McElroy, M. B.: Three-dimensional climatological distribution of tropospheric OH: Update and evaluation, Journal of Geophysical Research: Atmospheres, 105, 8931–8980, https://doi.org/10.1029/1999jd901006, 2000.

Stevenson, D. S., Zhao, A., Naik, V., O'Connor, F. M., Tilmes, S., Zeng, G., Murray, L. T., Collins, W. J., Griffiths, P., Shim, S., Horowitz, L. W., Sentman, L., and Emmons, L.: Trends in global tropospheric hydroxyl radical and methane lifetime since 1850 from AerChemMIP, Atmospheric Chemistry and Physics, https://doi.org/10.5194/acp-2019-1219, 2020.

Stevenson, D. S., Derwent, R. G., Wild, O., and Collins, W. J.: COVID-19 lockdown emission reductions have the potential to explain over half of the coincident increase in global atmospheric methane, Atmospheric Chemistry and Physics, 22, 14 243–14 252, https://doi.org/10.5194/acp-22-14243-2022, 2022.

Szopa, S., Naik, V., Adhikary, B., Artaxo, P., Berntsen, T., Collins, W. D., Fuzzi, S., Gallardo, L., Kiendler Scharr, A., Klimont, Z., Liao, H., Unger, N., and Zanis, P.: Short-Lived Climate Forcers. In Climate Change 2021: The Physical Science Basis.Contribution of Working Group I to the Sixth Assessment Report of the Intergovernmental Panel on Climate Change, Cambridge University Press, Cambridge, United Kingdom and New York, NY, USA, 817–922, https://doi.org/10.1017/9781009157896.008, 2021.

660 Taylor, K. E., Williamson, D., and Zwiers, F.: The sea surface temperature and sea ice concentration boundary conditions for AMIP II simulations, PCMDI Report 60 (25 pp.). Livermore, CA: Program for Climate Model Diagnosis and Intercomparison, Lawrence Livermore National Laboratory. Retrieved from https://pcmdi.llnl.gov/report/pdf/60.pdf, 2000.

Turner, A. J., Frankenberg, C., Wennberg, P. O., and Jacob, D. J.: Ambiguity in the causes for decadal trends in atmospheric methane and hydroxyl, Proceedings of the National Academy of Sciences, 114, 5367–5372, https://doi.org/10.1073/pnas.1616020114, 2017.

665 Turner, A. J., Fung, I., Naik, V., Horowitz, L. W., and Cohen, R. C.: Modulation of hydroxyl variability by ENSO in the absence of external forcing, Proceedings of the National Academy of Sciences, 115, 8931–8936, https://doi.org/10.1073/pnas.1807532115, 2018.

Turner, A. J., Frankenberg, C., and Kort, E. A.: Interpreting contemporary trends in atmospheric methane, Proceedings of the National Academy of Sciences, 116, 2805–2813, https://doi.org/10.1073/pnas.1814297116, 2019.

van Marle, M. J. E., Kloster, S., Magi, B. I., Marlon, J. R., Daniau, A.-L., Field, R. D., Arneth, A., Forrest, M., Hantson, S., Kehrwald, N. M.,
670 Knorr, W., Lasslop, G., Li, F., Mangeon, S., Yue, C., Kaiser, J. W., and van der Werf, G. R.: Historic global biomass burning emissions for CMIP6 (BB4CMIP) based on merging satellite observations with proxies and fire models (1750–2015), Geoscientific Model Development, 10, 3329–3357, https://doi.org/10.5194/gmd-10-3329-2017, 2017.

Wild, O., Zhu, X., and Prather, M. J.: Fast-J: Accurate Simulation of In- and Below-Cloud Photolysis in Tropospheric Chemical Models, Journal of Atmospheric Chemistry, 37, 245–282, https://doi.org/10.1023/a:1006415919030, 2000.

675 Wild, O., Voulgarakis, A., O'Connor, F., Lamarque, J.-F., Ryan, E. M., and Lee, L.: Global sensitivity analysis of chemistry–climate model budgets of tropospheric ozone and OH: exploring model diversity, Atmospheric Chemistry and Physics, 20, 4047–4058, https://doi.org/10.5194/acp-20-4047-2020, 2020.

Yin, Y., Chevallier, F., Ciais, P., Broquet, G., Fortems-Cheiney, A., Pison, I., and Saunois, M.: Decadal trends in global CO emissions as seen by MOPITT, Atmospheric Chemistry and Physics, 15, 13 433–13 451, https://doi.org/10.5194/acp-15-13433-2015, 2015.

680 Zhao, M., Golaz, J.-C., Held, I. M., Guo, H., Balaji, V., Benson, R., Chen, J.-H., Chen, X., Donner, L. J., Dunne, J. P., Dunne, K., Durachta, J., Fan, S.-M., Freidenreich, S. M., Garner, S. T., Ginoux, P., Harris, L. M., Horowitz, L. W., Krasting, J. P., Langenhorst, A. R., Liang, Z., Lin, P., Lin, S.-J., Malyshev, S. L., Mason, E., Milly, P. C. D., Ming, Y., Naik, V., Paulot, F., Paynter, D., Phillipps, P., Radhakrishnan, A., Ramaswamy, V., Robinson, T., Schwarzkopf, D., Seman, C. J., Shevliakova, E., Shen, Z., Shin, H., Silvers, L. G., Wilson, J. R., Winton, M., Wittenberg, A. T., Wyman, B., and Xiang, B.: The GFDL Global Atmosphere and Land Model AM4.0/LM4.0: 1. Simulation Char-
685 acteristics With Prescribed SSTs, Journal of Advances in Modeling Earth Systems, 10, 691–734, https://doi.org/10.1002/2017ms001208, 2018.

Zhao, Y., Saunois, M., Bousquet, P., Lin, X., Berchet, A., Hegglin, M. I., Canadell, J. G., Jackson, R. B., Hauglustaine, D. A., Szopa, S., Stavert, A. R., Abraham, N. L., Archibald, A. T., Bekki, S., Deushi, M., Jöckel, P., Josse, B., Kinnison, D., Kirner, O., Marécal, V., O'Connor, F. M., Plummer, D. A., Revell, L. E., Rozanov, E., Stenke, A., Strode, S., Tilmes, S., Dlugokencky, E. J., and Zheng, B.: Inter-
690 model comparison of global hydroxyl radical (OH) distributions and their impact on atmospheric methane over the 2000–2016 period, Atmospheric Chemistry and Physics, 19, 13 701–13 723, https://doi.org/10.5194/acp-19-13701-2019, 2019.

Zhao, Y., Saunois, M., Bousquet, P., Lin, X., Berchet, A., Hegglin, M. I., Canadell, J. G., Jackson, R. B., Deushi, M., Jöckel, P., Kinnison, D., Kirner, O., Strode, S., Tilmes, S., Dlugokencky, E. J., and Zheng, B.: On the role of trend and variability in the hydroxyl radical (OH) in the global methane budget, Atmospheric Chemistry and Physics, 20, 13 011–13 022, https://doi.org/10.5194/acp-20-13011-2020, 2020.

695 Zheng, B., Chevallier, F., Ciais, P., Yin, Y., Deeter, M. N., Worden, H. M., Wang, Y., Zhang, Q., and He, K.: Rapid decline in carbon monoxide emissions and export from East Asia between years 2005 and 2016, Environmental Research Letters, 13, 044 007, https://doi.org/10.1088/1748-9326/aab2b3, 2018.

Zheng, B., Chevallier, F., Yin, Y., Ciais, P., Fortems-Cheiney, A., Deeter, M. N., Parker, R. J., Wang, Y., Worden, H. M., and Zhao, Y.: Global atmospheric carbon monoxide budget 2000–2017 inferred from multi-species atmospheric inversions, Earth System Science Data, 11,
700 1411–1436, https://doi.org/10.5194/essd-11-1411-2019, 2019.